Title

Hyperfine Coupling Constants of the Mu-t-Butyl Radical in NaY and USY Compared with Similar Data in the Bulk and with Ab Initio Theory

Journal

The Journal of Physical Chemistry C, 117(32)

ISSN

1932-7447

Authors

Fleming, Donald G
Arseneau, Donald J
Bridges, Michael D
et al.

Publication Date

2013-08-15

DOI

10.1021/jp406879t

THE JOURNAL OF PHYSICAL CHEMISTRY C

Article

pubs.acs.org/JPCC

Hyperfine Coupling Constants of the Mu-*t*-Butyl Radical in NaY and USY Compared with Similar Data in the Bulk and with Ab Initio Theory

Donald G. Fleming* and Donald J. Arseneau†

TRIUMF and Department of Chemistry and †CMMS Facility at TRIUMF, University of British Columbia, Vancouver, British Columbia, Canada

Michael D. Bridges

Department of Chemistry and Biochemistry, California State University, Fullerton, California, United States

Ya Kun Chen and Yan Alexander Wang

Department of Chemistry, University of British Columbia, Vancouver, British Columbia, Canada

Supporting Information

ABSTRACT: A first complete μSR study of the T dependences of the (reduced) muon, $A'_\mu(T)$, and proton, $A_p(T)$, β-hyperfine coupling constants (hfcc) of the muoniated *t*-butyl radical is reported in the faujasitic zeolites NaY and USY, and the results are compared with similar data and with early EPR results in condensed bulk phases. The results are also compared with single-molecule UMP2 and DFT/B3LYP calculations in the bulk and in an NaY zeolite fragment of Si and O atoms with both OH- and H-capping. Muon hfcc are reported for the first time for the Mu-isobutyl radical in the bulk phase and are also compared with theory and with EPR data. The present results for the muon and proton hfcc of Mu-*t*-butyl in the bulk complement earlier work published elsewhere at higher temperatures but are extended here down to 5 K to facilitate comparisons with in vacuo theory at 0 K. Good fits to the data for both $A'_\mu(T)$ and $A_p(T)$ for Mu-*t*-butyl are found from the calculated hfcc in both the bulk and in NaY, assuming a Boltzmann-weighted energy dependence given by a simple twofold torsional potential, providing an estimate of the barrier to internal rotation. In contrast to the bulk data, there is no clear discontinuity seen in $A'_\mu(T)$ for Mu-*t*-butyl in NaY or USY at the melting point of isobutene, demonstrating the dominance of single-molecule guest−host interactions in the faujasite supercage. In contrast to the $A'_\mu(T)$ dependence in the bulk, there is no discontinuity seen for either of the proton hfcc, $A_{p,CH_3}(T)$ or $A_{p,CH_2Mu}(T)$, at the melting point, which also exhibit similar behavior in NaY, suggesting that its observation in the bulk for only the muon hfcc arises from a specific effect of the intermolecular interactions on the vibrational averaging of the muon hfcc. The measured muon hfcc for Mu-*t*-butyl in NaY fall below those in the bulk at low temperatures, indicating some transfer of electron spin density to the Na cation, which is confirmed by specific additional level-crossing resonances not observed in USY. The Na nuclear hfcc, $A_{Na}(T)$, follow a similar trend with temperature as $A'_\mu(T)$, with an estimate of the Na spin density at 0 K that also agrees well with theory.

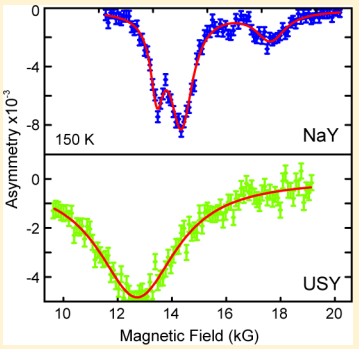

1. INTRODUCTION

An increasingly important isotopic spin probe of both hyperfine couplings and molecular dynamics and interactions of free radicals is the muonium (Mu = μ^+e^-) atom, dating from 1978.[1] The μ^+ is produced 100% spin polarized at a nuclear accelerator (TRIUMF in the present study), and this polarization can be transferred to a free radical by Mu addition reactions; here, $MuCH_2\dot{C}(CH_3)_2$ and $(CH_3)_2CMu\dot{C}H_2$ specifically, which are the muoniated analogs of the well-known *t*-butyl and isobutyl radicals,[2−8] are formed by a Mu addition to isobutene. The muon spin polarization in the radical can be sensitively monitored by the μSR technique,[3,4,9−16] which has an important advantage over other magnetic resonance techniques in that essentially only one radical at a time is detected, eliminating any concerns about radical−radical recombination reactions affecting the hyperfine coupling constants (hfcc) or line widths, which is often the case in EPR[2] and particularly in the geometric confines of zeolites.[17]

In a recent paper, the T dependences of both the muon, $A_\mu(T)$, and proton, $A_p(T)$, hfcc for the muoniated *s*-butyl radicals in bulk

Received: July 18, 2013
Published: July 19, 2013

   dx.doi.org/10.1021/jp406879t | J. Phys. Chem. C 2013, 117, 16523−16539

condensed phases were reported[12] and compared therein with in vacuo calculations,[18] giving good agreement with the experimental data. There have also been recent μSR papers measuring the hfcc and avoided-level-crossing (ALC) resonance line shapes in the faujasitic zeolites NaY, HY, and USY for the muoniated ethyl (MuC_2H_4)[16] and cyclohexadienyl (MuC_6H_6)[13] radicals, with the latter extending an earlier study in NaY,[19] as well as work reported elsewhere for the MuC_6H_6 radical in the zeolite ZSM-5.[20−22]

Zeolites, particularly their proton-exchanged forms, are important industrial catalysts[23−28] whose micropore structures faciliate channeling effects that can lead to the selective formation of transition states in catalytic reactivity.[24−27,29] Such states are often considered to be carbocation intermediates that are formed by proton-transfer reactions from the acidic zeolites, but there is still relatively little understood about the mechanisms occurring at the microscopic level in zeolite catalysis.[23,25,26] Important in this regard might be the free-radical intermediates formed by H-atom transfer reactions,[24,28,30] but there appears to be only a single EPR report of this, which examines the formation of C_6H_7 from γ-radiolysis processes in HZSM-5.[31] Because muoniated radicals are easily formed by Mu addition to guest molecules in zeolitic hosts, their study in these environments[13,16] can provide an important template for the equivalent H-atom reactions, which is one motivation for the present study, and in particular here for the Mu-*t*-butyl radical in NaY and USY.

Previous studies of muoniated alkyl radicals in bulk phases,[3,12,32,34] including the Mu-*t*-butyl radical,[3,4] and in faujasites[16,35] have established that the C−Mu bond, as a result of the light muon mass, adopts an eclipsed conformation at 0 K, which is aligned with the p_z orbital of the unpaired electron. The torsional barrier to internal rotation can then be determined by a measurement of the T dependence of the muon hfcc. It is also of interest to see what the effect of the zeolite framework might be on the internal rotation of the bulky Mu-*t*-butyl radical in comparison with earlier results for Mu-ethyl, where activation energies for torsional motion showed little or no effect upon interaction with the zeolite.[16]

The Mu-*t*-butyl radical also represents a good test case for ab initio single-molecule (in vacuo) calculational methods of both equilibrium geometry and β-proton hfcc for a more complex alkyl radical beyond the simplest ethyl radical[36−38] and beyond early studies of methyl rotation for *t*-butyl in the bulk[7,39] as well as here, for the first time, in the microcrystalline environments of NaY and USY, where the corresponding calculations in the bulk provide an important basis for comparison. Both spin unrestricted density functional theory (DFT) with the B3LYP density functional and UMP2 calculations, a similar methodology to that employed in ref 18, are also utilized here to calculate the muon and proton hfcc of Mu-*t*-butyl in NaY. The zeolite framework is represented by a six-membered cluster of Si and O atoms, with Na located in the center, to represent the S_{II} site[13,27,40] as in other theoretical studies in NaY,[35,41,42] with the Si atoms capped with either H atoms[41] or OH groups.[35]

2. EXPERIMENTAL BACKGROUND

2.1. Sample Preparation and Environment. Liquid isobutene was obtained from Aldrich Chemicals. The samples were loaded into target cells either in the bulk, as described in ref 12, or in the zeolite, as described in ref 16. Monitoring the change in pressure of the vapor allows a determination of the number of molecules adsorbed per supercage (SC), which ranged from 1 to 3 per SC, with an estimated loading error of 0.5. Prior to preparing each sample, several freeze−pump−thaw cycles were carried out to remove any dissolved O_2, which is known to cause extra line broadening in a μSR experiment because of electron spin exchange.[43,44] Each sample cell was sealed with a crimping tool prior to its removal from the vacuum system, with the sample then kept in a deep-freeze environment prior to use.

Each sample was mounted in a He-flow cryostat for temperature control and placed in a superconducting magnet that provided magnetic fields up to about 40 kG, aligned with the beam direction. The experiments were run on the M20 beamline at the TRIUMF cyclotron, which provides a spin-rotated muon beam, so that both longitudinal field (LF) and transverse field (TF) experiments could be run on the same sample. Spin-polarized surface muons pass through the thin metal target entrance window and stop within the isobutene sample, forming the muoniated radical. The temperature for the neat bulk samples was varied between 5 and 200 K, below the boiling point of the neat liquid, whereas in the zeolite samples temperatures up to 320 K were run. Temperature readings were monitored by two different thermocouples attached to the target cell, which typically gave consistent readings to within a degree, and were assumed to be the same temperature as that of sample. However, systematic errors in the cell temperatures between different run periods could be higher.

2.2. Basics of the μSR Technique. The μSR technique is well known,[3,9,11−13,15] so only a brief description is given here. The 100% spin polarization of the μ^+ is shared with the electron in the Mu atom, which is formed during the slowing processes of the muon in matter.[45,46] Muoniated radicals are formed by Mu addition reactions, and at high reactant concentrations, most of the initial polarization can be transferred with the muon spin to the radical.[47,48] In the decay process ($\mu^+ \rightarrow e^+\nu_e\bar{\nu}_\mu$), the positron is emitted preferentially along the muon spin direction regardless of its environment,[9,11,14−16] and it is detected by a counter array of plastic scintillators.

In a time-differential (TD) measurement in a TF, the muon asymmetry at the time of decay is given by

$$A(t) = \sum_i A_i e^{-\lambda_i t} \cos(\omega_i t + \phi_i) \tag{1}$$

where A_i, λ_i, ω_i, and ϕ_i are the initial asymmetry, relaxation rate, frequency, and initial phase for the ith environment, respectively. For a given Mu radical, typically observed in TFs of a few kG for alkyl radicals, there are three frequencies of interest: one corresponding to muons in diamagnetic environments (ν_D) and two radical frequencies, ν_{12} and ν_{34}, that correspond to the allowed transitions of the spin Hamiltonian.[11,47] These are usually most easily seen in Fourier transform (FT−μSR) spectra at the characteristic precession frequencies[3,9,11,16]

$$\nu_{12} = \left|\frac{1}{2}A_\mu - \nu_m\right| \quad \text{and} \quad \nu_{34} = \nu_m + \frac{1}{2}A_\mu \tag{2}$$

giving the isotropic muon-electron hfcc, A_μ, where

$$\nu_m = \frac{1}{2}([A_\mu^2 + (\nu_e + \nu_D)^2]^{1/2} - \nu_e + \nu_D) \tag{3}$$

with the Larmor frequencies $\nu_D = \omega_\mu/2\pi = \gamma_\mu B$ for diamagnetic muons (γ_μ = 0.01355 MHz/G) and $\nu_e = \gamma_e B$ for the electron (γ_e = 2.8025 MHz/G) in an applied TF, B.

The muon hfcc may also be found by the ALC−μSR technique, which additionally provides a direct determination of the nuclear hfcc, A_k (with k being H or Na here), in high

LFs.[3,11,15,16] An ALC signal appears as a dip in the time-integrated decay asymmetry at a specific resonant field, corresponding to the avoided crossing of eigenstates.[9,11,13] There are two principal ALC resonances that are of interest: a Δ_0 resonance represents a flip-flop exchange of spin polarization between the muon and a nuclear spin, from which the nuclear hfcc is determined, and a Δ_1 resonance that is a pure muon spin-flip, determining the muon hfcc. As aforementioned, A_μ can also be found from a TF−μSR experiment, a correspondence that provides a valuable identification of a Δ_1 line in ALC−μSR spectra.

Though hyperfine anisotropy and molecular reorientation of muoniated free radicals can give rise to asymmetric ALC line shapes, from which their molecular dynamics can be assessed,[9,11,16,19,20,44,49] it is the positions of the ALC resonances, $B_r(\Delta_1)$ and $B_r(\Delta_0)$, that are of prime importance here. These are well determined from the minimum of the Lorentzian fits carried out even for broad-line spectra,[12,15,16,19] giving the isotropic hfcc of interest, A_μ, from the minimum of the Δ_1 resonance, and A_k from the minimum of the Δ_0 resonance from eqs 4 and 5, respectively[11,15,16]

$$B_r(\Delta_1) = \frac{1}{2}\left|\frac{A_\mu}{\gamma_\mu} - \frac{A_\mu}{\gamma_e}\right| \quad (4)$$

$$B_r(\Delta_0) = \frac{1}{2}\left|\frac{A_\mu - A_k}{\gamma_\mu - \gamma_k} - \frac{A_\mu + A_k}{\gamma_e}\right| \quad (5)$$

with the nuclear gyromagnetic ratios γ_k being $\gamma_p = \gamma_\mu/3.183$ and $\gamma_{Na} = \gamma_p/3.912$ in addition to γ_μ and γ_e defined earlier. It will be convenient to express the muon hfcc in reduced units, $A'_\mu = A_\mu\gamma_p/\gamma_\mu = A_\mu/3.183$, which corrects for the change in the gyromagnetic ratios between the muon and proton and facilitates comparisons with theory and with EPR data.

3. EXPERIMENTAL RESULTS: $A'_\mu(T)$ AND $A_K(T)$

3.1. In the Bulk Phase. Two muoniated radical isomers can be formed from the Mu + $(CH_3)_2C{=}CH_2$ reaction: the common tertiary Mu-*t*-butyl radical and the primary Mu-isobutyl radical, which is much less common and is observed here for the first time, although only in the solid phase. Because both the muon and proton hfcc for Mu-*t*-butyl have been well determined earlier in the liquid phase by Percival et al. [3] and for $A_\mu(T)$ by Roduner et al.,[4] the present data in the bulk have mainly been acquired in the solid phase and importantly down to 5 K to provide a meaningful comparison with both the in vacuo calculations at 0 K and with the data in zeolites.

Example FT−μSR spectra in a TF of 3.45 kG are shown in Figure 1 at 75 K in the solid phase and at 142 K in the liquid phase, which is not far above the 133 K melting point of bulk isobutene. Although somewhat broadened because of hyperfine anisotropy,[16,19,49] the two strong transitions at ν_{12} = 174 MHz and ν_{34} = 280 MHz at 75 K are still quite sharp and directly give the muon hfcc A_μ = 454 ± 3 MHz (eq 2) for the Mu-*t*-butyl radical. The frequency at 134 MHz in Figure 1 (top) is identified as being the ν_{12} line of the Mu-isobutyl radical, with A_μ(*i*-Bu) = 368 ± 4 MHz, which is determined from eqs 2 and 3 and the diamagnetic frequency ν_D = 46.8 MHz, which is off scale in both plots.

In the liquid phase, the FT lines in Figure 1 show results only for the stronger Mu-*t*-butyl radical. Much sharper lines are seen than in the solid, which is partly due to the wider FT window of

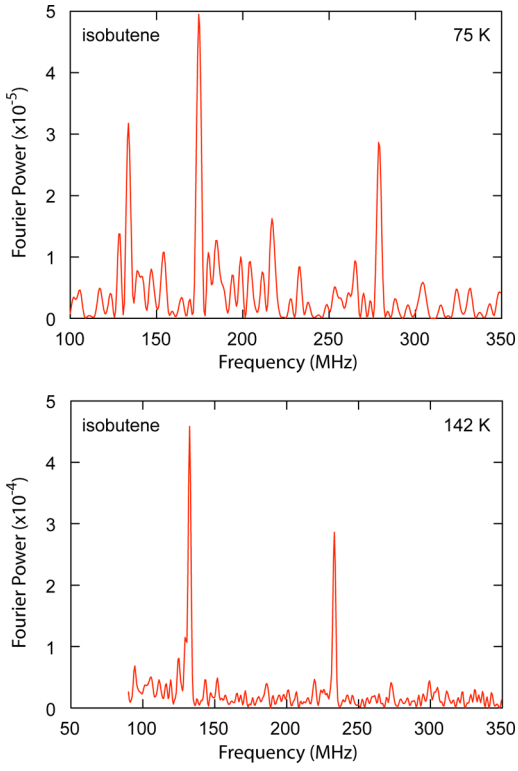

Figure 1. FT−μSR spectra of muoniated butyl radicals formed from Mu addition to isobutene at 75 K in the solid phase (FT time window 0.25 μs) and at 142 K in the liquid phase (FT time window of 0.50 μs) in a field of 3.45 kG. The strong signals shown in both spectra are the radical frequencies ν_{12} and ν_{34} for the Mu-*t*-butyl radical. The line at 134 MHz at 75 K is the ν_{12} transition for the Mu-isobutyl radical. The diamagnetic signal at ν_D = 46.8 MHz is off scale in both plots.

0.5 μs used here. The frequencies ν_{12} = 132 MHz and ν_{34} = 233 MHz give A_μ = 365 ± 2 MHz at 142 K, which is in agreement with an earlier value of 366 MHz interpolated from the data of Roduner et al.[4] A separate run at the same temperature in a different period gave A_μ= 360 MHz, which is consistent with that reported by Percival et al.[3] The reason for these few MHz discrepancies is unclear, but it is likely due to differences in the temperature or the temperature equilibration times in different sample environments.

Figure 2 shows ALC−μSR spectra over a range of temperatures but mainly in the solid phase. The red lines shown are Lorentzian fits with the background removed to better display the ALC resonances shown.[12,13,16,19] These spectra are dominated by the broad Δ_1 resonance for the Mu-*t*-butyl radical, starting at 18.09 kG at 5 K, giving the muon hfcc A_μ = 493 ± 2 MHz from eq 4. The much weaker downfield line barely seen at this temperature at 15.3 kG is attributed to the Δ_1 resonance for the muoniated isobutyl radical, giving A_μ = 417 ± 3 MHz. In addition to these Δ_1 resonances, two predominant Δ_0 resonances are expected for the *t*-butyl radical because of the eclipsed protons of the CH_3 groups and the staggered protons of $-CH_2Mu$. The Δ_0 resonance for the CH_3 protons is the nearby very broad line to the Δ_1 resonance at 20.8 kG at 5 K, giving A_{p,CH_3} = 105 ± 3 MHz from eq 5. A second and barely visible resonance near 24 kG is the Δ_0 line for the staggered CH_3 protons, giving A_{p,CH_3}= 37 ± 5 MHz, with the larger error reflecting the weak signal and the position of this resonance near the end of the scan. The Δ_0 resonance for the methylene protons

dx.doi.org/10.1021/jp406879t | J. Phys. Chem. C 2013, 117, 16523−16539

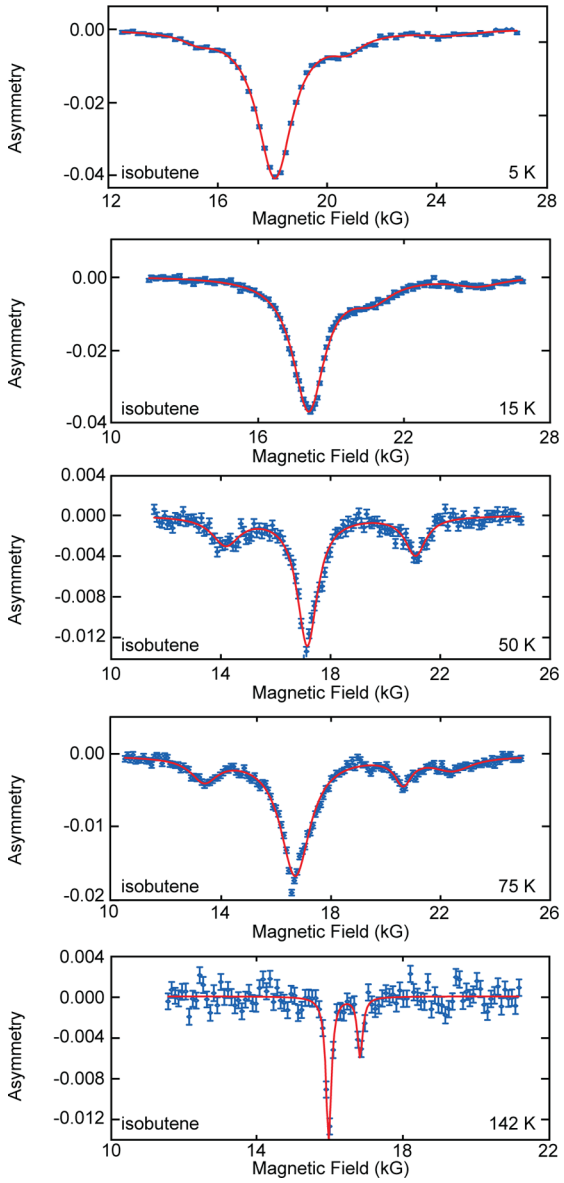

Figure 2. Representative ALC−μSR spectra with Lorentzian fits for the Mu-*t*-butyl radical in the solid phase and at 142 K (bottom) in the liquid phase, with the latter two scans recorded at the same temperatures as in Figure 1. The dominant (broad) resonances seen near 18 kG in the solid phase are the Δ_1 resonances for the muon hfcc of the Mu-*t*-butyl radical, and the weaker resonances at lower fields, near 14 kG, are the Δ_1 resonances for the Mu-isobutyl radical. The other fitted lines are Δ_0 resonances for the methyl and methylene proton hfcc.

is too weak to be seen here. Broad Δ_1 and Δ_0 resonances are seen over a range of temperatures in the solid phase.

In the isotropic environment of the liquid, the Δ_1 resonances have disappeared resulting from the reorientation of the radical on a time scale faster than the inverse of the hyperfine anisotropy (~50 ns). Consequently, the muon hfcc can only be determined from the TF data. The Δ_0 resonances for muoniated *t*-butyl are accordingly much sharper, as exemplified by the resonance positions seen at 142 K in Figure 2 (bottom) at 15.95 and 16.82 kG, giving the β-proton hfcc $A_{p,CH_3} = 62 \pm 1$ MHz and $A_{p,CH_2Mu} = 46 \pm 2$ MHz, respectively; both proton hfcc are in good agreement with the values reported in ref 3 at this temperature. The larger amplitude lower-field resonance for the six equivalent methyl protons is noteworthy, giving a clear 3:1 ratio as expected and is much clearer than in the solid-phase spectra where these amplitudes could be only qualitatively determined.

The averaged muon, $A_\mu(T)$, and proton, $A_p(T)$, hfcc for the *t*-butyl radical from the present study, determined from similar fits to data as seen in Figures 1 (or from fits to TD spectra, $A(t)$, from eq 1) and 2 are listed in Table 1 over temperatures from 5 to 200 K. The errors are combinations of both statistical and systematic uncertainties, arising from reproducibility in the data obtained in different run periods. The muon hfcc in the table are also given in reduced units, $A'_\mu(T)$, as defined earlier. Listed also are some data at higher temperatures for $A'_\mu(T)$ determined for Mu-*t*-butyl in solution[3] and over the full temperature range from the present study in NaY.

The values for $A'_\mu(T)$ from the present study of the Mu-*t*-butyl radical are shown as the cyan triangles in Figure 3, with the proton hfcc $A_p(T)$ plotted as the red and purple triangles in Figure 4. Also plotted in Figure 3 are data for $A'_\mu(T)$ for Mu-*t*-butyl from the earlier studies of Roduner et al.[4] in the liquid phase (light-brown squares) and by Percival et al.[3] in both phases (green squares). An important aspect of the present study is a comparison between ab initio theory and the experimental data for the hfcc of the Mu-*t*-butyl radical over a full range of temperatures in the bulk; therefore, it was necessary to establish the level of agreement with these earlier studies as well as to extend the data down to much lower temperatures (5 K) to provide a sound basis for comparison with the new data in NaY and USY. The marked discontinuity in the muon hfcc $A'_\mu(T)$ seen in both data sets at the 133 K melting point of bulk isobutene[3] (vertical dashed line) is noteworthy. Classical model fits (eq 9) to these $A'_\mu(T)$ data from DFT/B3LYP or UMP2 calculations of muon hfcc in the separate phases, both with EPR-III basis sets,[18] are shown by the cyan (DFT/B3LYP) line in the solid phase and the blue (UMP2) line in the liquid (extended to the solid phase, dashed blue line), which will be discussed below. The open triangles at 155.5 and 131.1 MHz at 0 K are from these calculations.

The $A'_\mu(T)$ results for the weakly formed Mu-isobutyl radical are plotted as the solid black triangles in Figure 3 (not listed in Table 1). The black line is a fit to eq 9 from the UMP2/EPR-III calculations of the muon hfcc[18] with a 0 K value of 130 MHz. For comparison, the proton hfcc for the (single) C−H bond of the unsubstituted isobutyl radical from early EPR measurements[7,8] are plotted as well (solid green circles) and are fit to the B3LYP/EPR-III calculations for the $A_H(T)$ dependence, mainly in the liquid phase (extended into the solid, dashed green line), with a value of 140 MHz at 0 K.[18]

The μSR and EPR data for the β-proton hfcc of the *t*-butyl radical are plotted in Figure 4. The unsubstituted radical has mainly C_{3V} symmetry,[39] with pyramidal distortion at the radical center at low temperatures evident as well[3,50] (Table 2). For a fully planar radical, all protons would be equivalent, with the hfcc expected to be T independent. However, early EPR studies in different matrix or bulk environments have established this down to only 77 K,[5,7,8,31,50] as indicated in Figure 4 by the two representative EPR data points shown (dark-green solid circles). The earlier μSR data for the unsubstituted β-methyl protons of Mu-*t*-butyl[3] (green squares) are also T independent down to ~100 K, which is essentially within the errors of the EPR values.

The hfcc for the eclipsed methyl protons, $A_{p,CH_3}(T)$, from the current μSR study in the bulk phase are the solid red triangles in Figure 4. Near the melting point, these reproduce the trend in the

dx.doi.org/10.1021/jp406879t | J. Phys. Chem. C 2013, 117, 16523−16539

Table 1. Muon and β-Proton hfcc for the *t*-Butyl Radical Formed from Isobutene in Bulk and in NaY

T (K)	A_μ [a]	A'_μ [b]	A_{p,CH_3} [c]	A_{p,CH_2Mu} [c]	A'_μ (NaY) [b]	A_{p,CH_3} (NaY) [c]	A_{p,CH_2Mu} (NaY) [c]
5	493(2)	155(1)	106(3)		149(2)		
15	493(2)	155(1)	103(4)	27(4)			
30	493(2)	154(2)			149(2)		
50	487(2)	153(2)	73(4)	29(4)			
60					148(2)		
75	464(3)	146(2)	70(3)	36(5)			
90	453(1)	142(1)	63(3)		147(1)		
100	338(1)	138(1)	71(3)	40(4)			
120	420(1)	132(1)			138(2)		
130	411(1)	129.0(5)	62(2)				
132	408(2)	128(1)					
135	369.5(5)	116.0(5)			128(1)	61(3)	
142	363(2)	114(1)	62(2)	46(2)			
150	362.6(5)	113.9(5)			122(1)	60(2)	42(5)
175	350.5(5)	110.0(5)					
180					114(1)	60(2)	
200	338.5(5)	106.4(5)					
210					110.3(5)		
240 [d]	304(1)	96.3(5)			101(2)	63(3)	51(3)
255 [d]	302(1)	94.7(5)			99.5(5)	62.0(15)	51(2)
270 [d]	297(1)	93.3(5)			98(2)	60(3)	52(4)
298 [d]	289(1)	90.8(5)			95(2)	63(1)	54(2)
320					92.6(5)	62(1)	56(3)

[a]Muon hfcc found from either the TF data, the positions of the FT peaks (Figure 1), the TD fits (eq 1), or the positions of the Δ_1 resonances (Figure 2), which were calculated from eq 4. The errors are discussed in the text. [b]The reduced muon hfcc, $A'_\mu = A_\mu/3.184$, in both the bulk and in NaY. [c]β-proton hfcc for the eclipsed protons of the terminal CH_3 groups and the staggered protons of $-CH_2Mu$ found from the positions of the Δ_0 ALC resonances (Figures 2 and 5) for the *t*-butyl radical, which were calculated from eq 5. [d]Representative values for $A_\mu(T)$ interpolated from Table 1 in ref 3. The errors were assessed to be higher than those given in this Article.

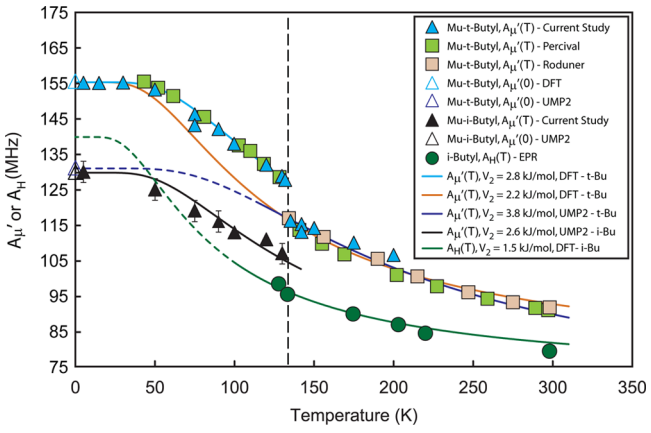

Figure 3. Temperature dependences of the muon hfcc, $A'_\mu(T)$, for the Mu-*t*-butyl (solid cyan triangles, present study; shaded green squares, ref 3; and shaded brown squares, ref 4) and Mu-isobutyl radicals (solid black triangles, present study). Also shown are EPR data points for the unsubstituted isobutyl radical (solid green circles). The colored fit lines are based on classical calculations for different torsional barriers. Several theory points are plotted on the *y* axis at 0 K and these along with the fitted lines for both the DFT/B3LYP-EPRIII calculations from Table 3 or the UMP2/EPR-III calculations from ref 18 are discussed in the text. The vertical dashed line denotes the melting point of bulk isobutene at 133 K. The sharp discontinuity in $A'_\mu(T)$ for the muoniated *t*-butyl radical is noteworthy.

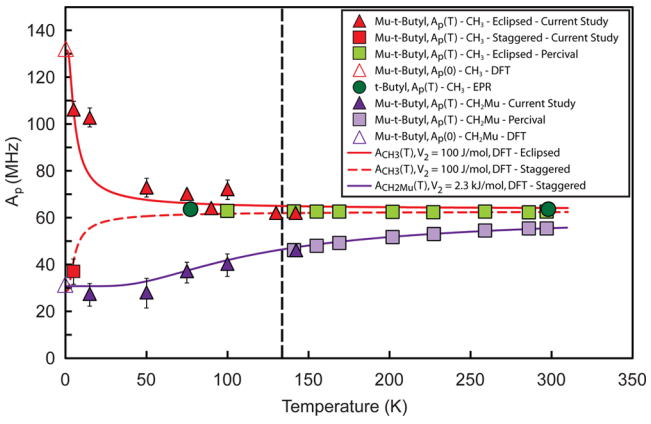

Figure 4. Temperature dependences of the β-proton hfcc, $A_p(T)$, for the muoniated and unsubstituted *t*-butyl radicals in the bulk. The upper data points and plots are for the CH_3 protons of muoniated *t*-butyl (present data, solid red triangles; data from ref 3, shaded green squares) and the lower data points and plots are for $-CH_2Mu$ (present data, solid purple triangles; data from ref 3, light purple squares). The two solid green circles are representative of the early EPR measurements for the methyl protons of the unsubstituted radical. The solid red line is a classical fit to the T dependence, $A_{p,CH_3}(T)$, for the eclipsed methyl protons from the DFT/B3LYP-EPRIII calculations of the proton hfcc in Table 3, whereas the dashed red line is a similar fit to the staggered methyl protons for the same (100 J/mol) torsional barrier. The solid purple line is a fit to $A_{p,CH_2Mu}(T)$ for the staggered methylene protons, which is also from the DFT/B3LYP-EPRIII hfcc calculations in Table 3.

data from ref 3 well, but they begin to deviate at the lower temperatures, particularly at 15 and 5 K, showing markedly increased hfcc that are well outside the error bars and scatter in the data. (The Δ_0 resonances in Figure 2 are very broad in the solid phase, giving proton hfcc with expanded errors.) The solid red line shown is a fit of eq 9 to these $A_{p,CH_3}(T)$ data from the

dx.doi.org/10.1021/jp406879t | *J. Phys. Chem. C* 2013, 117, 16523−16539

B3LYP/EPR-III-calculated hfcc in Table 3, giving the 0 K value of 131.6 MHz shown by the open triangle. The fit gives a very small torsional barrier of only 100 ± 10 J/mol, as demanded by the steep slope seen in the data. The dashed red line in this figure is a similar calculation for the corresponding staggered methyl protons (eq 10), assuming the same fitted barrier. These are very weakly populated, so only a single data point (red square at 5 K) could be determined. Note that in contrast to $A'_\mu(T)$, these $A_{p,CH_3}(T)$ data do not exhibit any discontinuity at the bulk phase transition.

In comparison with the unsubstituted radical, the Mu atom introduces an inequivalence in the protons of the β-CH_2Mu group, which gives rise to staggered proton hfcc that increase with increasing temperature, as shown by the lower data points in Figure 4 (the inverse trend to that exhibited by both $A'_\mu(T)$ and $A_{p,CH_3}(T)$). The light-purple squares are from ref 3, whereas the darker-purple triangles are the present data, establishing the trend much better down to 5 K. The solid purple line shown is a fit of these $A_{p,CH_2Mu}(T)$ data for both data sets to the model of eq 10 from the B3LYP/EPR-III calculations of the proton hfcc in Table 3. Interestingly, the methylene protons also do not exhibit any discontinuity at the 133 K melting point of isobutene.

3.2. In NaY and USY. The polycrystalline zeolite environment broadens both the TF/FT−μSR lines and ALC−μSR resonances compared to the bulk, particularly at the lower temperatures, because of hyperfine anisotropy. Example ALC spectra for the Mu-*t*-butyl radical in NaY are plotted in Figure 5 for a loading of three isobutenes per SC. Similar ALC plots comparing the spectra for NaY and USY are shown in Figure 6 at temperatures of 90, 150, and 240 K. The solid lines are again fits to background-corrected Lorentzian line shapes for each peak, as in Figure 2.

The very broad line seen at ∼17.5 kG at 30 K in Figure 5 is the Δ_1 resonance for the muon. There is a barely discernible resonance at ∼14 kG, which we believe is the Δ_0 resonance for the Na nuclear hyperfine coupling and is obscured by the tail of the Δ_1 line. The muon resonance is noticeably sharper at 90 K at a field of ∼17.2 kG. The distinct resonances seen at ∼15.4 kG at 90 K in Figure 5 and most clearly at ∼13.4 kG at 150 K are the Na Δ_0 lines, which are seen also as a shoulder at ∼11.4 kG in the scan at 240 K, although they are obscured by the shifted position of the muon resonance at ∼11.8 kG here. Note that the Δ_1 resonances in NaY extend to temperatures well above the bulk melting point of 133 K, although they become much weaker at higher temperatures where $A'_\mu(T)$ was determined mainly from the TF data.

The Na Δ_0 resonances were generally observed over the full temperature range, although with more uncertainty from broader ALC lines at the lowest temperatures. To first order, we may expect the peak areas of Δ_0 ALC lines to scale approximately as $|A_\mu A_k|$,[10] which is qualitatively the case for the Na resonances here. The observation of these resonances is clear evidence for the binding of the Mu-*t*-butyl radical to the cation in NaY, evidence that was lacking for the MuC_6H_6 radical in ref 13. The typically weaker resonances seen at the higher fields above the Δ_1 lines in Figure 5 are mainly the Δ_0 resonances for the CH_3 protons, although the upper weak resonance seen at ∼13.1 kG at 298 K is for the $-CH_2Mu$ protons. This narrow scan was intentionally chosen with smaller field steps to better resolve both the methyl and particularly methlyene resonances; the expected intensity ratio of 3/1 is clearly observed here. Both

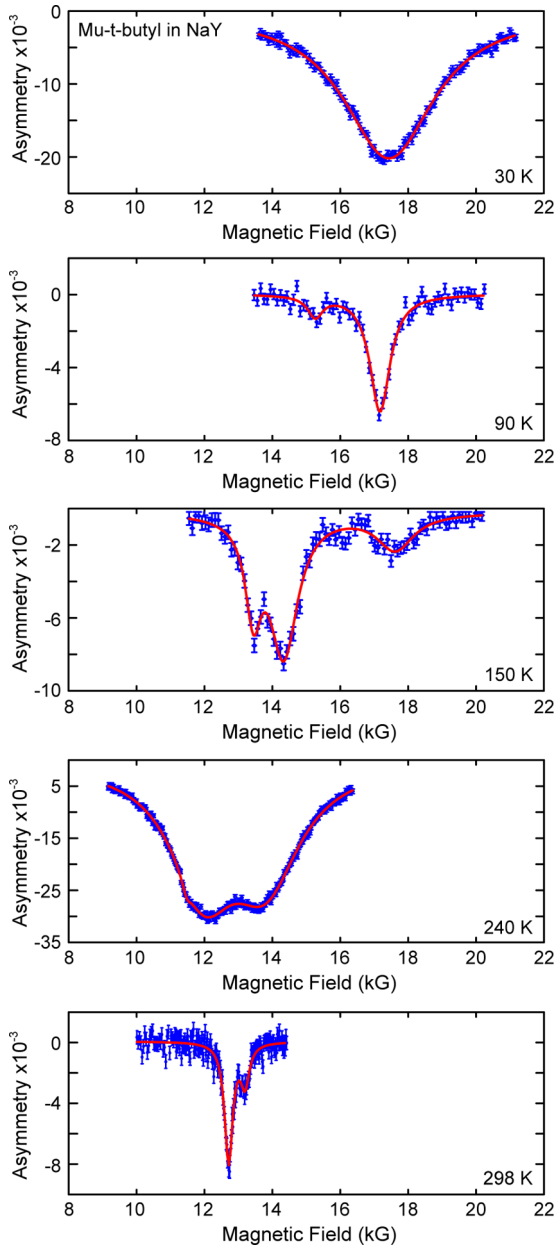

Figure 5. Representative ALC−μSR spectra with Lorentzian fits to the background-corrected spectra for the Mu-*t*-butyl radical formed from isobutene for a loading of three isobutenes per SC in NaY at selected temperatures. These spectra are typically broader and hence less distinct than those for the corresponding plots in the bulk phase (Figure 2), but in like manner they are dominated by the Δ_1 resonance, which extends up to much higher temperatures than in the bulk. Both the Na Δ_0 and muon Δ_1 resonances are too weak to be seen in the low statistics scan at 298 K.

proton resonances are much less distinct in USY (Figure 6) because of the extended tails of the very broad Δ_1 lines.

There are no signs of any Na resonances in USY (Figure 6), as was expected. The Δ_1 resonances that dominate each scan are also generally much broader in USY than in NaY, indicating more motion of the *t*-butyl radical sampling a higher degree of hyperfine anisotropy, which is similar to what was seen for the MuC_6H_6 radical in USY.[13] The Δ_1 resonances shift to lower fields with increasing temperature in both frameworks, reflecting the temperature dependence in $A'_\mu(T)$, and are consistently found at

dx.doi.org/10.1021/jp406879t | J. Phys. Chem. C 2013, 117, 16523−16539

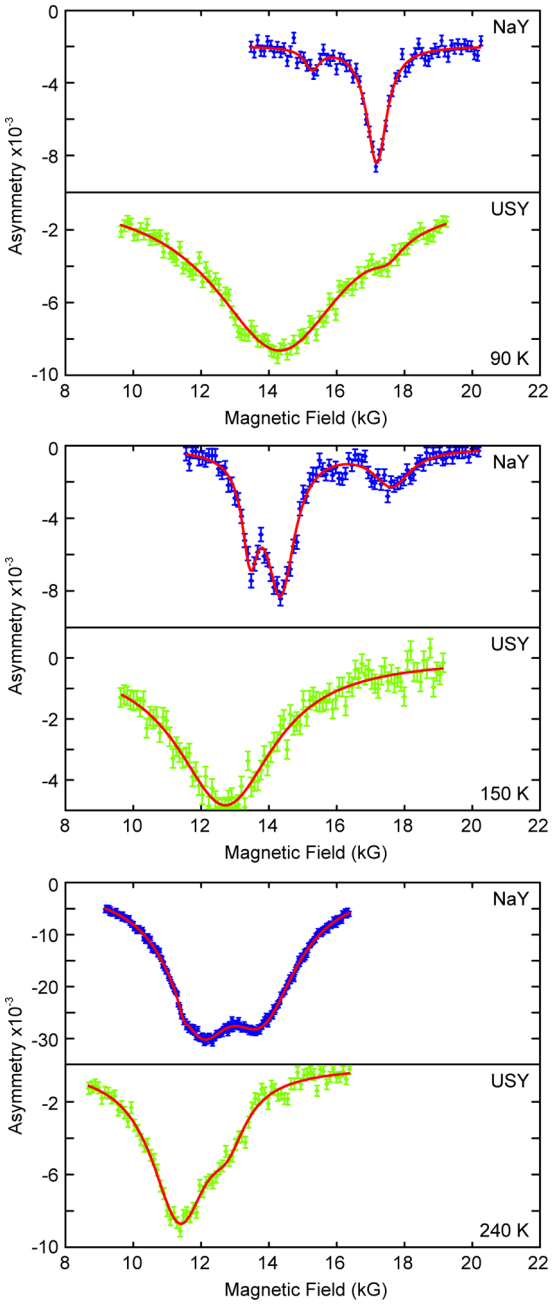

Figure 6. Representative ALC−μSR spectra with Lorentzian fits for the Mu-*t*-butyl radical formed from Mu addition to isobutene at a loading of three isobutenes per SC in NaY (from Figure 5) compared with similar plots in USY at 90, 150, and 240 K. The USY scans are dominated by much broader Δ_1 lines that are also shifted to lower fields than in NaY. The Na Δ_0 resonances seen in NaY are absent in the USY data. There are also weaker lines seen at higher fields in USY at 90 and 240 K, which are the Δ_0 resonances for the methyl protons.

lower fields in USY than in NaY, corresponding to lower muon hfcc. The results have been tabulated in Table 1 for NaY (only) and are plotted for both NaY (red data points) and USY (green) in Figure 7 for loadings of mainly three isobutenes per SC and are compared therein with results from the bulk (Figure 3), which is shown by the solid cyan (to 133 K) and blue fit lines, with the latter extended through the solid. Some data were also taken in NaY at one isobutene per SC (240, 270, and 300 K) and are plotted in Figure 7 but are not distinguished in the plot because

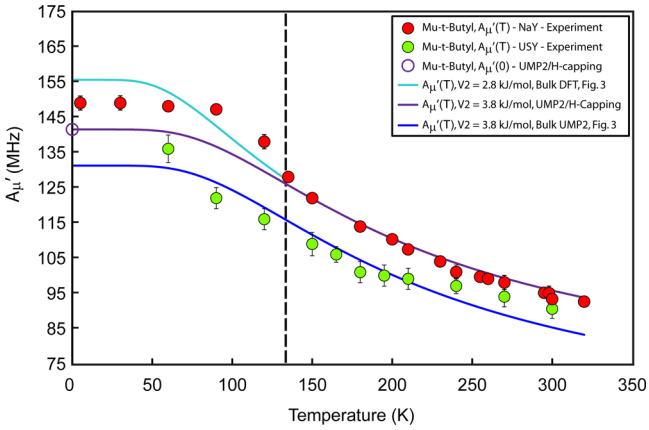

Figure 7. Plot of the reduced muon hfcc, $A'_\mu(T)$, for the Mu-*t*-butyl radical in NaY (red data points) and in USY (green points) compared with the earlier fitted B3LYP/EPR-III lines for results in the bulk solid phase (cyan line, up to 133 K) and from the UMP2/EPR-III calculations in the liquid phase (blue line) (both taken from Figure 3). The purple line is a fit of eq 9 to the $A'_\mu(T)$ in the NaY data, assuming the UMP2/EPR-II calculations with H-capping from Table 4, with $A'_\mu(0)$ = 141.5 MHz, indicated by the open purple circle, and giving a fitted barrier of 3.8 kJ/mol.

these values did not differ significantly from those of the nearby points at three isobutenes per SC.

The purple line in Figure 7 is a fit of eq 9 to the $A'_\mu(T)$ data for Mu-*t*-butyl in NaY from the UMP2/H-capping calculations of Table 4, with $A'_\mu(0)$ = 141.5 MHz. Although falling below the data at the lower temperatures, the fit at the higher temperatures is good. (The B3LYP/EPR-III calculations from Table 3 are well above the data, which is a similar trend as in the bulk in Figure 3.) The blue line is not a fit to the USY data but is taken from the UMP2/EPR-III fit to the $A'_\mu(T)$ data in the bulk liquid from Figure 4 and accounts quite well for the USY data over its temperature range. Note that the $A'_\mu(T)$ values for USY fall well below those found in NaY over most of the temperature range and are much closer in fact to the similar values in the bulk. Significantly, there is no clear discontinuity in $A'_\mu(T)$ at any temperature in either NaY or USY, demonstrating the importance of guest−host interactions in the faujasite supercage. The decrease seen in muon hfcc at low temperatures in NaY compared to the bulk (cyan line from Figure 3) suggests some transfer of electron spin density from the radical to the cation, which is in accord with the observation of Na Δ_0 resonances.

The proton hfcc, determined from the Lorentzian fits to the Δ_0 lines and eq 5, are plotted for NaY in Figure 8. These could only be determined at the higher temperatures. Similar results were found in USY, albeit with larger errors and only at a few temperatures and are not plotted. The eclipsed protons for $A_{p,CH_3}(T)$ in NaY are shown as the green diamonds in Figure 8, whereas the red triangles are methyl hfcc from the bulk (Figure 4) along with the two EPR points (green circles) from that figure. The green line is is taken from the earlier fit to the bulk data, with the same fitted torsional barrier of V_2 = 100 J/mol, although here with $A_{p,CH_3}(0)$ = 139.5 MHz (open triangle) from the B3LYP/OH-capping calculations from Table 3. The H-capping calculations ($A_{p,CH_3}(0)$ of 143.8 MHz) give a trend line that is shifted slightly higher for this barrier (not plotted).

The staggered hfcc for $A_{p,CH_2Mu}(T)$ in NaY are the cyan diamonds in Figure 8, with the purple triangles from the bulk data

dx.doi.org/10.1021/jp406879t | J. Phys. Chem. C 2013, 117, 16523−16539

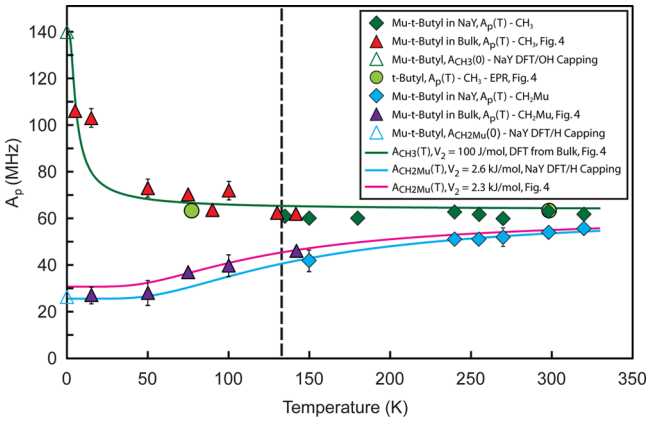

Figure 8. Plots of the proton hfcc for CH_3 (green diamonds) and CH_2Mu (cyan diamonds) for the Mu-*t*-butyl radical in NaY along with the earlier data in the bulk at low temperatures from Figure 4 (red and purple triangles). The upper green line is the same as the fitted line from Figure 4 for $A_{p,CH_3}(T)$ but for a 0 K intercept of 139.5 MHz (open green triangle) from the B3LYP/EPR-III calculations of Table 3 with OH-capping. The solid green circles are the EPR points from Figure 4. The cyan line is a fit of eq 10 to the data for $A_{p,CH_2Mu}(T)$ in NaY from the B3LYP/EPR-III calculations from Table 3 for H-capping (26.7 MHz at 0 K, open cyan triangle), giving a fitted barrier of V_2 = 2.6 kJ/mol. The magenta line is the fitted result for $A_{p,CH_2Mu}(T)$ from Figure 4.

of Figure 4. Here, the cyan line is a fit of eq 10 to these methylene proton hfcc in NaY only, from the B3LYP/H-capping calculations from Table 3 (26.7 MHz at 0 K). The OH-capping calculations gave essentially the same fit. A similar outcome is seen in Figure 9. The magenta line in Figure 8 is taken directly from the fit to the bulk data in Figure 4, which makes clear that the fit to the NaY data is below the results for $A_{p,CH_2Mu}(T)$ in the bulk, in concert with the transfer of electron spin density from the *t*-butyl radical to the cation seen in the $A'_\mu(T)$ data in Figure 7.

3.3. Sodium Resonances. The Na hfcc, $A_{Na}(T)$, are plotted in Figure 9. The solid blue line is a semiempirical fit on the basis

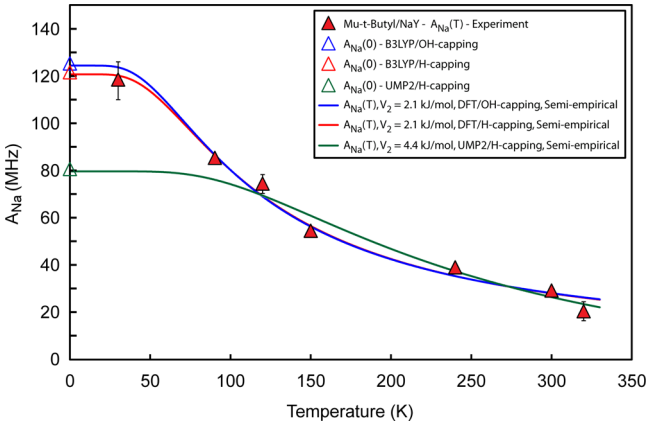

Figure 9. Plot of the *T* dependence of the Na hfcc, $A_{Na}(T)$, mainly for a loading of three isobutenes per SC (the point at 290 K is at one isobutene per SC). The blue and red fit lines are semiempirical using the B3LYP/EPR-III calculations from Table 3 with OH- and H-capping, giving 0 K values of 124.2 (open blue triangle) and 120.7 MHz (open red triangle), with both giving the same torsional barrier of 2.1 ± 0.2 kJ/mol. The green line is also a semiempirical fit, but it is from the UMP2/EPR-II calculations with H-capping from Table 4, with a 0 K value of 79.8 MHz (open green triangle), and gives a poor fit to the data.

of the same model as in the bulk for $A'_\mu(T)$ from the B3LYP/III calculations with OH-capping from Table 3, but with a fitted parameter for the second term of eq 9. The red trend line is a similar result from the H-capping calculations, with both giving equally good fits to the data. The central assumption here, justified below, is that the amount of electron spin density transferred from the central carbon to the Na cation decreases with increasing temperature in a like manner to that of the dihedral angle dependence for the muon hfcc of the Mu-*t*-butyl radical, $A'_\mu(T)$. The green line is from the UMP2/EPR-II H-capping calculation from Table 4 and fails to account for the data point at 30 K, even with its large error.

4. ASPECTS OF THEORY: $A'_\mu(T)$ AND $A_K(T)$

4.1. Background to Previous Calculations in the Bulk. The comparisons with theory in this Article for the muon and proton hfcc of the muoniated *t*-butyl radical in both bulk phases and in the zeolite environments for NaY and USY are in accord with recently published results for in vacuo (single molecule at 0 K) DFT/B3LYP and UMP2 calculations of the hfcc for the ethyl and, mainly, *s*-butyl radicals[18] carried out within the Born−Oppenheimer (BO) approximation, partly with EPR-II but mainly with EPR-III basis sets.[51−53] The degree of spin contamination in the UMP2 wave functions is small. Vibrational averaging corrections,[51,54] which are known to be particularly important for the muon hfcc given the large effect of zero-point energy (ZPE) upon substitution of the much lighter (factor of 9) Mu atom in a C−H bond,[34,55−57] were treated by a simple ansatz in which the C−Mu bond was stretched to 1.076 times the equilibrium C−H bond distance, discussed in ref 18, and was based on methods developed by Boehm et al.[56] and Lounila et al.,[58] with hfcc calculations then carried out on this modified but static geometry. Stretching the C−Mu bond weakens it compared to C−H, effectively enhancing the electron spin density at the muon, giving rise to a larger hfcc and thereby approximating the effect of vibrational averaging on the muon hfcc.

4.2. Barriers to Internal Rotation: The *T* Dependence of *β*-hfcc. In muoniated radicals, where Mu replaces H in a methyl group, as in Mu-*t*-butyl, the barrier to internal rotation is expected to be entirely vibrationally induced,[3,4,11,12,16,18,32−35] with the C−Mu bond adopting an eclipsed geometry with respect to the p_z orbital of the unpaired electron (upe), resulting in a maximum hfcc at 0 K that also reflects the effect of vibrational averaging that is modeled by the ansatz described earlier. Concomitantly, the protons in $-CH_2Mu$ adopt a staggered geometry, exhibiting a minimum hfcc at 0 K. With increasing temperature, the larger vibrational amplitude of the C−Mu bond results in it rotating away from its favored conformation, decreasing its hfcc, $A'_\mu(T)$, with the opposite effect seen for the methylene protons. The measurement of this *T* dependence provides a determination of the torsional barrier hindering internal rotation. For the unsubstituted CH_3 protons of the Mu-*t*-butyl radical, a high proton hfcc resulting from eclipsed C−H bonds at 0 K is also expected.

For *β*-substituted alkyl radicals, the torsional barrier depends on the dihedral angle (θ) between the p_z orbital of the upe and the direction of the C−H (or C−Mu) bond, $V_B(\theta)$, and can be determined from the potential energy difference between conformations of maximum and minimum total energy.[3,6,7,33,36,39] Although detailed ab initio calculations of torsional barriers for alkyl radicals have been carried out,[33,36,39,59] most are historic now and the results can be

dx.doi.org/10.1021/jp406879t | J. Phys. Chem. C 2013, 117, 16523−16539

unreliable because of the methods that were used as well as the general difficulty of accurately determining total energies.

Thus, in comparison with experiment, recourse is often made to phenomenological models for the determination and interpretation of torsional barriers, first established by Fessenden,[7] in which $V_B(\theta)$ is assumed to have twofold angular symmetry for a pair of rigidly rotating alkyl groups of the form

$$V_B(\theta) = \frac{1}{2}V_2(1 - \cos 2\theta) \tag{6}$$

which assumes a planar radical center (symmetry about p_z for $\pm\theta$ rotations) and also ignores molecular interactions and vibrations about the minimum,[59] which is effectively then also a single molecule approximation. Though both local threefold and sixfold potentials better describe the dihedral angle dependence for methyl groups in unsubstituted alkyl radicals,[33,39] the presence of the muon in the −CH2Mu group introduces an asymmetry in methyl rotation such that even though these higher torsional symmetries have been considered for Mu-substituted radicals,[3,32,33,60] they do not offer any real improvement in fitted results compared to the simple potential of eq 6 for the torsional motion affecting the C−Mu bond, which is consistent with its natural twofold rotational symmetry for alignment with the p_z orbital of the upe at 0 K.

For the unsubstituted methyl group of Mu-*t*-butyl, although threefold (or sixfold) symmetry seems a natural choice, as for the unsubstituted radical, the effect of torsional couplings with other modes[59] are unknown for muoniated radicals. One could expect these to be appreciable given the huge effect of ZPE on the vibrational averaging on the muon hfcc. It is arguably as reasonable then to continue to employ eq 6 to model the T dependence of methyl rotation in Mu-*t*-butyl as it is for any other phenomenological form. It is also only sensible to apply the same model for torsional motion of different alkyl groups in the same radical, so that the fitted barriers can be compared on the same basis.

If the interchange rate between different rotational conformers, with hfcc $A_\beta(\theta_j)$ at angle θ_j, is faster than the difference in their hyperfine frequencies, then the observed value of the β-hfcc at a given temperature, $A_\beta(T)$, can be written as a Boltzmann-weighted average over torsional energy states E_j

$$A_\beta(T) = \frac{\sum_j A_\beta(\theta_j)e^{-E_j/k_BT}}{\sum_j e^{-E_j/k_BT}} \tag{7}$$

By fitting experimental data for the T dependence of β-hfcc to the form of eq 7, the barrier height V_2 can be determined. Although an inherently high-T approximation, this thermal-averaging method has enjoyed wide success over a range of temperatures, as cited in ref 12. For muoniated radicals, it was first employed by Ramos et al. to determine V_2 for the Mu-ethyl radical in the liquid phase[32] and later by Percival et al.[3] to determine V_2 for the Mu-*t*-butyl in both the liquid and solid phases, with both assuming the McConnell description of β-hfcc.[2,3,6,7,16,32,60]

In the spirit of these phenomenolgical approaches, we have used the classical model outlined by Krusic et al.[6] for determining $A_\beta(T)$ in which the torsional energy levels E_j of eq 7 are replaced by $V_2(\theta)$ from eq 6, giving the form

$$A_\beta(T) = \frac{\sum_j A_\beta(\theta_j)\, e^{-V_2(\theta_j)/k_BT}}{\sum_j\, e^{-V_2(\theta_j)/k_BT}} \tag{8}$$

where the $\sum_j$ is over angles for different equilibrium conformations and where $A_\beta(\theta_j)$ are found from ab initio calculations of the β-hfcc at these conformations. Although in principle this sum should be evaluated knowing $A_\beta(\theta_j)$ at a multitude of angles on the torsional surface, a qualitative determination of the torsional barrier height that explains the observed T dependence for $A_\beta(T)$ can be found by selecting the three equilibrium angles, $\theta_j = 0$ and $\pm120°$, for the basic C_3 rotational symmetry of a methyl group, with hfcc calculated at these angles.[12,18] Thus, from ref 12 for eclipsed C−H bonds at 0°, eq 8 reduces to

$$A_\beta(T) = \frac{A_\beta(0) + [A_\beta(120) + A_\beta(-120)] \times e^{-0.75V_2/k_BT}}{1 + 2e^{-0.75V_2/k_BT}} \tag{9}$$

and for staggered (±120°) C−H bonds

$$A_\beta(T) = \frac{A_\beta(120) + [A_\beta(0) + A_\beta(-120)] \times e^{-0.75V_2/k_BT}}{1 + 2e^{-0.75V_2/k_BT}} \tag{10}$$

To be useful, a model should be simple. There is only one fitted parameter here: the torsional barrier height, V_2. Although any quantum effects arising from the light muon mass that might be exhibited by $A'_\mu(T)$ would obviously not be accounted for by this simple classical model, these may also be seen in the experimental results, in which case accurate fits to the data even from a simple model can be instructive.

4.3. Methodology and Geometries for *t*-Butyl in NaY.

Isolated single-molecule calculations have been carried out in Gaussian09[61] using a 64-bit compiler, with a similar methodological approach as described in ref 18 and were briefly commented on above. (These earlier calculations used Gaussian03 on a 32-bit compiler.) The B3LYP hybrid density functional was used to construct the DFT Hamiltonian,[62,63] with EPR-III basis functions[53] employed for calculations of the hfcc for the *t*-butyl radical and with both OH-capping and H-capping for the NaY environment. Comparisons are also made with UMP2 calculations in the zeolite environment but for only an EPR-II basis set with H-capping.

Zeolites are aluminosilicate frameworks with a unit cell consisting of eight sodalite cages (too small to accommodate alkyl radicals) and eight supercages (SC),[23,27,40] where in NaY the extra-framework Na cations compensate the negative charge of each AlO_2 link in a 3D array of tetrahedral bonding. The experimental NaY sample in this study had a Si/Al ratio of about 3.5, whereas that for USY was about 6.8.[12,13] Each SC is joined to four others via 12-ring windows (W) of Si or Al atoms and 12 bridging O atoms of ∼7.5 Å in diameter, leading to SC pore sizes of ∼13 Å in diameter that easily accommodate large radicals such as *s*-butyl,[12] cyclohexadienyl,[13] and *t*-butyl (here).

Only a small part of the unit cell is used to model the host−guest interaction between the *t*-butyl radical and the NaY framework. As is commonly done, this is taken to be a six-membered ring of tetrhedrally bonded Si/Al and O atoms with a Na cation at its center,[35,41,42] representing the location of the 'SII' cation within a SC.[27,40] (A diagram showing this for Mu-cyclohexadienyl in the same NaY fragment may be seen in ref 13). Although including the Al either directly or via a charge-averaged T-atom model[35,41] is important if the goal of the calculation is to model the effect of Brønsted acid sites, this is arguably less important in the calculation of hfcc. Accordingly, we have adopted this simpler fragment model Si_6O_6Na, as in the

dx.doi.org/10.1021/jp406879t | J. Phys. Chem. C 2013, 117, 16523−16539

calculations of ref 41 for the binding of ethene to cation sites in NaY. Each Si atom is capped by either H atoms[41] or hydroxyl groups.[35] The electronic structure calculation is simpler for H-capping, although OH-capping better preserves the total charge of the missing Si atoms. The effect of both cappings are compared for the present B3LYP/EPR-III calculations of the hfcc for the Mu-*t*-butyl in NaY in Table 3 below.

To calculate the muon hfcc of Mu-*t*-butyl in the NaY environment, we adopted the same ansatz of elongating the C−Mu bond by 1.076 from its equilibrium geometry for C−H, which was utilized above for the calculations of $A'_{\mu}(T)$ in the bulk (Figure 3), to compensate partially for the dynamical effect of vibrational averaging for the C−Mu bond. Although the degree of this C−Mu bond stretching could be slightly different in NaY, we have not explored this because we expect that it would not be a significant effect given the close similarity in the data seen in the two environments (Figure 7). The framework structure of USY is more complex,[13] and no hfcc calculations were carried out for this.

In the NaY calculations, the Pople 6-31+G** basis functions were used for the Na^+ and the six-membered ring fragment, including the capping of Si by H or OH, to determine the hfcc of the *t*-butyl radical in the C_4H_9·NaY environment. During geometry optimization involving NaY, the position of all of the atoms in the zeolite fragment were fixed, whereas those of the capping atoms (with the same fixed directions as those of the Si or O atoms in the O−Si−O links of the original zeolite but with flexible bond lengths for the capping H atoms) and of the *t*-butyl radical were allowed to move. For comparison, we have also studied the structure of the complex composed of a bare Na^+ and the radical (C_4H_9·Na^+), where the 6-31+G** basis set was also used for the Na^+ cation.

Some key geometric parameters for the *t*-butyl radical complexed with bare Na^+ and with NaY are summarized in Table 2 for the B3LYP/EPR-III calculations for both H- and OH-capping. Similar results are shown in Table S1 for the UMP2 calculations for H-capping with an EPR-II basis for *t*-butyl, with comparisons also given there for an EPR-III basis set for C_4H_9·Na^+. There are generally only small differences seen in these geometrical parameters between the B3LYP and UMP2 calculations in comparison with the in vacuo results and in particular for tBu·NaY for either H- or OH-capping. There is little change between H- and OH-capping as well because both are pointing in the same direction as in the original zeolite framework (away from the cation). The biggest effects are on the dihedral angle, which is determined by the intersection of the two planes for the backbone carbon atoms (180° for a planar carbon skeleton). This is already nonplanar for the uncomplexed radical, indicating a pyramidal angle of 22°, but it becomes even more so upon interacting with either a bare Na^+ or *t*-butyl·NaY for the zeolite fragment, indicating that pyramidal distortion is significantly enhanced in the NaY supercage.

Table 2. Geometric Parameters for *t*-Butyl in Different Environments from B3LYP/EPR-III Calculations[a]

parameter	*t*-butyl	*t*-butyl·Na^+	*t*-butyl·NaY (H-capping)	*t*-butyl·NaY (OH-capping)
Ċ−CH_3	1.491	1.499	1.498	1.499
C−H (e)	1.103	1.101	1.101	1.101
∠ C−Ċ−C	118.8	117.7	117.4	117.1
dihedral angle	158.2	150.3	148.3	147.0
C−H (s)	1.093	1.092	1.091	1.091
Ċ−Na		2.548	2.650	2.708

[a]The 2nd column gives the in vacuo calculation for the unsubstituted radical, the 3rd column is for its interaction with a bare Na^+, the 4th column gives the effect of the interaction with the NaY fragment for the H-capping of the Si atoms, and the 5th column gives this for OH-capping. The notations '(e)' and '(s)' in the first column refers to the eclipsed and staggered conformations, respectively. The distances are in angstroms, and the angles are in degrees.

This distortion effect results in less spin density spreading from the radical center to the peripheral H atoms compared to the planar radical. On this basis alone, we could expect a reduced hfcc for particularly the muon hfcc of Mu-*t*-butyl in NaY compared to the bulk at low temperatures. However, this purely geometrical effect is offset by the interaction of the radical with the NaY environment, as can be seen from the calculations of hfcc in Tables 3 and 4.

As noted, the methodology followed here is similar to that for calculations in the bulk and is generally as follows: (i) obtain a single optimized geometry for an isolated *t*-butyl radical (first in the bulk and then in the NaY environment) at 0 K, (ii) determine the hfcc of both the methyl and methylene protons from the equilibrium geometries found, and for the muon from the ansatz for the C−Mu bond stretched by a factor of 1.076, with calculations then carried out on this modified but static 0 K geometry, and (iii) fit the T dependence of the data to a Boltzmann average over the torsional energy states using model eqs 9 or 10 and the ab initio calculations of hfcc at 0 K to obtain a value of the torsional barrier, V_2, both in the bulk and in NaY.

4.4. Electronic Binding Energies of *t*-Butyl in NaY. A table of the electronic binding energies (BEs), which are inherently negative quantities, for both the B3LYP and UMP2 calculations is given in Table S2 for the interaction of the *t*-butyl radical with a bare cation (top three entries) and for the two capping environments of the NaY fragment. In a manner consistent with the shorter radical−Na^+ distance seen from the geometries in Table 2, the largest calculated BEs are for the *t*-butyl·Na^+ interaction in comparison with those for *t*-butyl·NaY, which are in fact relatively weak, varying between only 3.9 and 7.2 kcal/mol. These are much weaker than the estimates suggested in ref 13 for the binding of the Mu-cyclohexadienyl radical to NaY at up to ∼25 kcal/mol. There are large differences in dipole moments, however, between cyclohexadienyl, ∼ 0.47 D,[42] and *t*-butyl, which is estimated to be only ∼0.2 D.

In the study from ref 13, the line widths for the Δ_1 (muon) resonance in NaY, which inform about motional dynamics, were followed up to 470 K, revealing a much stronger binding of C_6H_6 in NaY than in USY, but in the present study of the hfcc of Mu-*t*-butyl, the highest temperature was only 320 K, so it is not possible to draw any firm conclusions from these data about the magnitudes of the BEs given in Table S2. Still, we can infer from the ALC line widths in Figures 5 and 6 that the BE for *t*-butyl is considerably weaker in USY compared to NaY, which is in like manner to that seen for MuC_6H_6.[13] (We remark that the B3LYP calculations of BEs for *t*-butyl in HY reported in ref 35 appear to be far too high compared to NaY, with the latter agreeing reasonably well with those found here, despite the different basis sets employed.)

4.5. Calculated Hyperfine Coupling Constants. The calculated single-molecule hfcc from Gaussian09 for the unsubstituted *t*-butyl radical and for the proton and muon hfcc of the muoniated *t*-butyl radical, as well as the ^{13}C hfcc, are shown in Table 3 for the B3LYP/EPR-III calculations for both H- and OH-capping of the NaY fragment and in Table 4 for the UMP2/

Table 3. B3LYP/EPR-III-Calculated Hyperfine Coupling Constants (in MHz) for *t*-Butyl and Mu-*t*-Butyl in Different Environments[a]

calculation	**Mu**	**Ċ**	**CMuH$_2$**	**CMuH$_2$** (e)	**CMuH$_2$** (s)	**CH$_3$**	**CH$_3$** (e)	**CH$_3$** (s)	**Na**
t-butyl		121.2				−26.5	133.2	30.3	
t-butyl (geometry from *t*-butyl·Na$^+$)		140.9				−21.7	128.2	26.5	
t-butyl·Na$^+$		88.2				−14.3	151.1	27.8	140.8
t-butyl·NaY (H-capping)		93.0				−13.3	145.7	26.7	121.9
t-butyl·NaY (OH-capping)		94.6				−10.4	141.7	26.0	125.5
Mu-*t*-butyl	155.5	120.3	−25.5		29.1	−25.8	131.6	29.8	
Mu-*t*-butyl·Na$^+$	174.4	87.3	−13.6		27.3	−13.7	149.1	27.4	140.1
Mu-*t*-butyl·NaY (H-capping)	168.1	92.7	−12.3		26.1	−12.6	143.8	26.3	121.0
Mu-*t*-butyl·NaY (OH-capping)	163.7	93.7	−9.1		25.4	−10.0	139.5	25.2	124.4
Mu-*t*-butyl (120)	34.7	121.2	−29.1	132.3	30.7	−26.8	133.2	30.4	
Mu-*t*-butyl·Na$^+$ (120)	31.2	138.7	−16.6	150.4	28.1	−14.6	151.1	27.9	138.7
Mu-*t*-butyl·NaY (120) (H-capping)	29.9	94.2	−15.5	145.0	26.7	−13.5	145.7	26.8	120.4
Mu-*t*-butyl·NaY (120) (OH-capping)	31.5	95.2	−12.8	141.4	26.1	−10.8	141.2	26.0	124.1

[a]Determined from Gaussian09.[61] The atom for which the hfcc is calculated is shown in bold type. For both the CMu**H**$_2$ and C**H**$_3$ environments, (e) and (s) refer to eclipsed (0°) and staggered (120°) conformations. The entries in the 2nd row are for *t*-butyl with the same geometry as for its interaction in NaY but in the absence of any interaction with the cation, whereas the 3rd row shows the effect of these interactions with the bare cation. The 4th and 5th rows show the difference in the NaY environment with H- and OH-capping, respectively.

Table 4. UMP2/EPR-II-Calculated Hyperfine Coupling Constants (in MHz) for *t*-Butyl and Mu-*t*-Butyl in Different Environments[a]

calculation	**Mu**	**Ċ**	**CMuH$_2$**	**CMuH$_2$** (e)	**CMuH$_2$** (s)	**CH$_3$**	**CH$_3$** (e)	**CH$_3$** (s)	**Na**
t-butyl		168.2				−25.7	113.9	22.1	
t-butyl·Na$^+$		106.5				−16.6	128.9	20.6	86.8
t-butyl·NaY (H-capping)		108.3				−17.8	128.3	21.0	80.3
Mu-*t*-butyl	128.1	166.8	−22.9		20.8	−24.9	112.6	21.6	
Mu-*t*-butyl·Na$^+$	143.9	105.1	−14.7		19.7	−16.0	127.5	20.2	86.7
Mu-*t*-butyl·NaY (H-capping)	141.5	107.0	−16.8		20.0	−15.9	127.7	20.2	79.8
Mu-*t*-butyl (120)	23.7	168.3	−27.8	113.1	22.0	−25.9	113.9	22.1	
Mu-*t*-butyl·Na$^+$ (120)	22.0	107.1	−18.4	128.3	20.4	−16.7	128.9	20.6	85.8
Mu-*t*-butyl·NaY (120) (H-capping)	23.3	108.7	−20.4	126.4	20.5	−17.7	129.2	20.6	79.7

[a]H-capping only. See the caption for Table 3.

EPR-II calculations for H-capping only. The Mulliken spin densities for H-capping are given in Tables S3 and S4, respectively. The effect of a change in basis set for the UMP2 calculations of hfcc is shown in Table S5 for the *t*-butyl interacting with a bare cation only. In these tables, the atom for which the hfcc has been calculated is indicated in bold. Of particular interest here and in comparison with the current experiments, are the results for the eclipsed (e) and staggered (s) C−H bonds in C**H**$_3$ presented, in addition to the results for C−Mu (labeled '**Mu**').

There are some fairly significant differences seen in the calculated hfcc for the *t*-butyl radical in Tables 3 and 4 resulting from synergistic changes in the molecular interactions and geometry caused by the NaY environment inducing a redistribution of the spin density at the nucleus. We have attempted to assess these largely opposing effects by the B3LYP/EPR-III calculations shown in the top five rows of Table 3 for the unsubstituted *t*-butyl radical. Although it is mainly the ^{13}C hfcc (not measured here) that are most affected by changes in the environment, there are also significant changes in the hfcc for the methyl protons, C**H**$_3$, particularly for the eclipsed conformation.

The effect of geometry alone is quite appreciable, as can be seen by comparing the hfcc in the bound geometry of the radical in the NaY environment, but in the absence of any interaction with the Na cation, shown in the second row of Table 3 and the freely optimized radical geometry shown by the in vacuo calculations in the first row. The effect of the interaction between the radical and the charge of the cation is shown for *t*-butyl·Na$^+$ in the third row, which largely reverses the trend noted earlier resulting from just the geometry. Note the large increase seen in the proton hfcc for C**H**$_3$ (e), which is more so than for C**H**$_3$ (s).

Also noteworthy is the relatively large nuclear hfcc of 140.8 MHz that appears for the *t*-butyl·Na$^+$ interaction (third row in Table 3), reflecting a transfer of spin density from the central Ċ atom to the cation (Tables S3 and S4). The effect of H- or OH-capping further alters these trends, although at only the few percent level. The same general trends are seen for the Mu-*t*-butyl radical (row 6 and above), for which specific comparisons are made with the μSR data in Figures 7−9, as discussed later.

Similar trends are also seen in Table 4 for the UMP2/EPR-II H-capping calculations. The most obvious difference between these two methodologies is that the UMP2-calculated hfcc are uniformly less compared to B3LYP, by as much as 20% in some cases, and by about twice that for the Na hfcc. This trend to reduced hfcc in the UMP2 calculations seems to be a general outcome for alkyl radicals[12,18] and is found also in the interpretation of the data for $A'_\mu(T)$ for Mu-*t*-butyl in the bulk (Figure 3), also discussed later.

Because the B3LYP calculations of hfcc were carried out in NaY with an EPR-III basis set, whereas the UMP2 calculations utilized EPR-II, it raises the question of how sensitive the UMP2/EPR-II-calculated hfcc are to a change of the basis set for the *t*-

dx.doi.org/10.1021/jp406879t | J. Phys. Chem. C 2013, 117, 16523−16539

butyl radical. The full UMP2/EPR-III calculations for the NaY fragment did not converge, but we were able to compare the effect of a change in the basis set for the *t*-butyl·Na^+ interaction, as shown in Table S5. In comparison with the entries in Table 4, it is again the ^{13}C hfcc that are the most dramatically affected, but more importantly here both the muon and proton hfcc increase by only about 3% on average, with a similar decrease seen in the Na hfcc. Because these changes are of the same order as the experimental errors in the μSR data for Mu-*t*-butyl in NaY (Figures 7−9), we conclude that the comparisons made between the data and the calculated UMP2/EPR-II hfcc in Table 4 will not be significantly compromised.

5. DISCUSSION: THEORY AND EXPERIMENT

5.1. $A'_\mu(T)$ and $A_p(T)$ for *t*-Butyl and Isobutyl in the Bulk.

The results for the T dependences of the (reduced) muon, $A'_\mu(T)$, and proton, $A_p(T)$, hfcc for the muoniated *t*-butyl radical in the bulk and their comparison with some EPR data and with theory are shown in Figures 3 and 4. Less complete data for the Mu-isobutyl radical are also shown in Figure 3. At low temperatures, from near 50 to 5 K, $A'_\mu(T)$ remains constant at the maximum value of the muon hfcc for the eclipsed C−Mu bond, particularly for the Mu-*t*-butyl radical (cyan triangles). An eclipsed conformation is also indicated by the T dependence for the proton hfcc of the single C−H bond of the isobutyl radical (green circles and dashed line) and for the methyl protons of the muoniated *t*-butyl radical in Figure 4 (red triangles and fitted line).

For Mu-*t*-butyl, a fit of the simple function of eq 9 to the $A'_\mu(T)$ data in the solid phase from the B3LYP/EPR-III calculations of the muon hfcc given in Table 3 ($A_\mu'(0)$ = 155.5 MHz) is shown by the cyan line and gives an excellent fit to both data sets, with a torsional barrier V_2 = 2.8 ± 0.2 kJ/mol, which is a bit lower than that reported in ref 3 (3.4 kJ/mol) from a different method performed over a more limited temperature range. The discontinuity seen in $A'_\mu(T)$ at the 133 K melting point of isobutene is a clear indication of the effects of the intermolecular interactions on the muon hfcc in the isobutene environment, which is possibly enhanced by the predominately planar nature of the *t*-butyl radical.[18] This cannot be accounted for by thermal-average models such as those represented by eq 7 or eq 9. The excellent agreement noted between the in vacuo B3LYP calculations and experiment for $A'_\mu(T)$ in the solid phase may then be fortuitous, as though these calculations mimick the effect of lattice interactions.

Percival et al.[3] fit their Mu-*t*-butyl hfcc in the liquid phase assuming the same value for $A'_\mu(0)$ as in the solid, which is tantamount to assuming the same potential minimum in both phases. It follows that the different T dependences seen in Figure 3 in the solid and liquid phases are due to differing distributions of the torsional states. The orange fitted line in Figure 3 makes the same assumption and gives an equally good fit to all of the data, including the earlier data of Roduner et al.[4] in the liquid phase (light-brown squares) and with the same torsional barrier of V_2 = 2.2 ± 0.2 kJ/mol as that found in ref 3. The higher barrier found from both studies in the hindered environment of the solid ensures more limited vibrational excursions near 0 K, which is in accord with the observation of a broader plateau region in Figure 3. It is worth remarking that the early calculations of the torsional barrier for methyl rotation in *t*-butyl[50] gave ∼2.7 kJ/mol, which is in good agreement with the fitted barriers found here from eq 9. Pyramidal inversion of the carbon skeleton at the α-carbon[3,39,50] may also be contributing to $-CH_2Mu$ rotation in the liquid phase.

An alternative point of view is that intermolecular interactions in the bulk influence not only the distribution of torsional states but also the spin density itself, thereby directly enhancing the muon hfcc near 0 K. This is implied by the UMP2-calculated fit of eq 9 to the data for $A'_\mu(T)$ in the liquid phase in Figure 3 (blue line) extended into the solid phase (dashed line), with a value at 0 K of 131.1 MHz.[18] This is much lower than the B3LYP-calculated value of 155.5 MHz that agrees well with the muon hfcc data at 5 K and gives an excellent fit to all three data sets in the liquid phase, with a higher fitted barrier, V_2 = 3.8 ± 0.3 kJ/mol, consistent with the more shallow slope of the liquid-phase data. The point here is that UMP2-calculated muon hfcc are in accord with the comparisons carried out in ref 18 for the ethyl radical in the absence of evidence for intermolecular interaction effects on the hfcc (no discontinuity is seen in $A'_\mu(T)$ at the phase transition for ethene[16]), which give the best agreement with both ab initio theory[37,38,56] and experiment for the muon hfcc of the Mu-ethyl radical, supporting the alternate view here that the $A'_\mu(T)$ dependence seen for Mu-*t*-butyl in the solid phase may be largely due to lattice interactions.

The black triangles and fitted line in Figure 3 are the $A'_\mu(T)$ data for the muoniated isobutyl radical, $(CH_3)_2C\,Mu\dot{C}H_2$. The fit, again to the classical model of eq 9, utilizes the UMP2-calculated muon hfcc of ref 18, and it too is in excellent agreement with the experimental trend, with a torsional barrier V_2 = 2.6 ± 0.3 kJ/mol. In contrast to the possibly fortuitous agreement noted above for Mu-*t*-butyl in the solid phase from the B3LYP-calculated hfcc, the DFT calculations here do not agree with the experiment for Mu-isobutyl, giving a 0 K value of 160 MHz, which is well above the measured value and thus supports the rationale for the UMP2 calculation here. It may be that molecular interactions affecting the muon hfcc in the solid phase are not as important for the less-planar carbon skeleton of the primary Mu-isobutyl radical compared to the Mu-*t*-butyl radical, but this could only be confirmed by TF−μSR data for Mu-isobutyl in the liquid phase.

The green line in Figure 3 is a fit of eq 9 to early published EPR data for the proton hfcc for the single C−H bond of the unsubstituted isobutyl radical (green circles)[6−8] from the B3LYP/EPR-III calculations of proton hfcc,[18] which is also in accord with the aforementioned comparisons between theory and experiment for the ethyl radical. Although there is no data in the solid, the value at 0 K of 140 MHz from these extrapolated DFT-calculated hfcc (dashed green line) gives a torsional barrier of V_2 = 1.5 ± 0.2 kJ/mol from the fit shown, which is in accord with conventional wisdom that the barrier for $A'_\mu(T)$ should be higher as a consequence of the ZPE-enhanced vibrational contributions to the C−Mu bond.

For the muoniated *t*-butyl radical, there are two β-proton environments (for the unsubstituted CH_3 groups and for the substituted $-CH_2Mu$ group), with their hfcc $A_{p,CH_3}(T)$ (red triangles) and $A_{p,CH_2Mu}(T)$ (purple triangles) plotted in Figure 4. On the basis of the EPR data indicated there (green circles) and from the earlier μSR measurements of Percival et al.[3] over a similar temperature range (green squares), along with the well-known EPR results for the ethyl radical,[64] we expected to see a T-independent methyl proton hfcc for the Mu-*t*-butyl radical, $A_{p,CH_3}(T)$. However, the present data, even allowing for its relatively high level of scatter, clearly show that this is not the

dx.doi.org/10.1021/jp406879t | J. Phys. Chem. C 2013, 117, 16523−16539

case, with these hfcc increasing dramatically with decreasing temperature below ∼50 K.

The solid red line is a fit of eq 9 to both μSR data sets for $A_{p,CH_3}(T)$ from the B3LYP-calculated proton hfcc of Mu-*t*-butyl from Table 3 (131.6 MHz at 0 K), giving a fitted barrier of only 100 ± 10 J/mol. Although one may question the simple model potential of eq 6 used here, the steep slope in the data itself dictates an unusually small torsional barrier. Interestingly, the broad plateau seen in the muon hfcc in Figure 3 is in sharp contrast to the T dependence seen for the eclipsed proton hfcc of unsubstituted CH_3, suggesting that the flat T dependence for $A'_\mu(T)$ as $T \rightarrow 0$ over a 50 K range could be a manifestation of quantum effects specifically affecting the alignment of the C−Mu bond. The lone data point at 5 K in Figure 4 (solid red-square) is for the staggered CH_3 protons, and the broken red trend line is calculated from eq 10, assuming the same torsional barrier of 100 J/mol as for the eclipsed protons.

The purple line in Figure 4 is a fit of eq 10 to both μSR data sets for the staggered protons of $-CH_2Mu$, again from the B3LYP-calculated hfcc (Table 3), and is essentially the mirror image of the decrease seen for $A'_\mu(T)$ in Figure 3. The 0 K intercept of 30.7 MHz (open purple triangle) and fitted line are in excellent agreement with the data, with a fitted torsional barrier $V_2 = 2.3 \pm 0.2$ kJ/mol. This is somewhat lower but not inconsistent with the DFT fits for $A'_\mu(T)$ in Figure 3, giving $V_2 = 2.8 \pm 0.2$ kJ/mol. (These would be strictly the same for only rigid-rotor rotation.) The high-temperature "free rotor" limiting value of 64.3 MHz from these B3LYP calculations for $A_{p,CH_3}(T)$ is also in excellent agreement with the trend in the data. In contrast, the UMP2 calculations give poor agreement at all temperatures, which again is consistent with the trends discussed in ref 18.

Another noteworthy feature in Figure 4 is that there is no discontinuity seen at the bulk melting point for the proton hfcc of either $A_{p,CH_3}(T)$ or $A_{p,CH_2Mu}(T)$, with the latter in particular being in marked contrast to $A'_\mu(T)$ for the same $-CH_2Mu$ group in Figure 3. This dramatic difference in behavior between the muon and proton hfcc seen at the phase transition suggests a fundamental difference in the intermolecular interactions that specifically impact the muon in the C−Mu bond, perhaps because of the effect that these interactions have on the zero-point vibrational averaging of the muon hfcc and which is reflected as well in the differing trends seen at the lowest temperatures for $A'_\mu(T)$ (Figure 3) and $A_{p,CH_3}(T)$ (Figure 4).

5.2. $A'_\mu(T)$ and $A_p(T)$ for Mu-*t*-Butyl in NaY and USY. The muon hfcc, $A'_\mu(T)$, for the Mu-*t*-butyl radical in NaY and USY are plotted in Figure 7 and show a smooth T dependence in both NaY (red data points and purple fitted line) and USY (green points and blue line), which is in contrast to the discontinuity seen at the bulk phase transition of 133 K in Figure 4. Although there is perhaps a hint of some discontinuity just past the bulk melting point (vertical line) in NaY, this is not seen in USY, and because guest−host interactions are stronger in NaY we are persuaded that this is not a real effect. The smooth trends seen in the data for $A'_\mu(T)$ in both NaY and USY demonstrate that at a loading of 3/SC it is guest−host interactions at single binding sites that dominate in the zeolite supercage, which is the opposite limit from the many-body interactions that appear to be manifest by the discontinuity seen in $A'_\mu(T)$ in the bulk. Stated otherwise, there is no equivalent to molecular freezing resulting from the guest−guest interactions of isobutene between supercages at this loading (which may be contributing for benzene at the highest loadings of 6/SC in USY[13]).

Because the equilibrium geometries of Table 2 point to an enhanced contribution from the pyramidal distortion of Mu-*t*-butyl in the zeolite supercage, the absence of any clear discontinuity in $A'_\mu(T)$ in NaY (or USY) also echoes an earlier suggestion that its observation in the bulk could be partially due to facile pyramidal inversion at the radical center in the liquid phase, which is in accord with the rather large distortion from planarity seen in Table 2 for the uncomplexed radical. This could well be hindered in the zeolite supercage.

This difference between the bulk and the NaY data also provides the key to the comparisons with theory here. Because guest−guest interactions play little or no role in the zeolite SC at the loadings of interest, it reasonable to continue to employ the single-molecule model of eq 6 to describe the torsional barrier. The purple line in Figure 7 is a fit of eq 9 to the $A'_\mu(T)$ data for NaY, assuming the UMP2/EPR-II H-capping calculations of Table 4 (0 K value of 141.5 MHz), giving a torsional barrier $V_2 = 3.8 \pm 0.3$ kJ/mol. This gives a reasonable overall account of the data, particularly in the liquid phase, although it falls below the experiment by about 5% in the solid phase. The fitted barrier for $-CH_2Mu$ rotation here is about 30% higher in NaY than the average of the fitted results in the bulk (Figure 3), suggesting that there could be an additional steric effect arising from the internal rotation of the bulky methyl groups in the geometric confines of the supercage. As to be expected from the calculations of ref 18, in the absence of lattice interactions, the B3LYP/EPR-III calculated muon hfcc from Table 3 give worse overall fits to the data (not plotted). However, it is of some interest to compare these results with the earlier B3LYP-calculated values of Ghandi et al.[35] with a less extensive basis set, giving $A'_\mu(0) = 130$ MHz in NaY, which is about 30% below the DFT results here in Table 3 ($A'_\mu(0) = 163.7$ MHz). It is likely that this difference is mainly due to a different treatment of the vibrational averaging contributions to the muon hfcc in ref 35.

At the lowest temperatures, the trend to lower muon hfcc for $A'_\mu(T)$ in NaY compared to the bulk (cyan line from Figure 3) seen in Figure 7, indicating a transfer of electron spin density to the Na^+ (Figure 9), is in contrast to earlier studies of both the Mu-ethyl[16] and Mu-cyclohexadienyl[13] radicals in NaY, where the muon hfcc near 0 K are actually about 20% higher than in the bulk and where there is also no evidence for any Na hfcc. The low-temperature trend in Figure 7 is reversed at the higher temperatures up to about 250 K, with the muon hfcc in NaY being well above those in the bulk (blue line from Figure 3). The data for $A'_\mu(T)$ for Mu-*t*-butyl in NaY are also well above those in USY, which closely parallel the bulk data up to this same temperature. This close similarity is further evidence for weaker guest−host interactions with bridging hydroxyl groups in the USY supercage, which is seen also for the Mu-cyclohexadienyl radical in a comparative study in NaY and USY.[13] Because there are no extra-framework cations in USY, it is reasonable to expect more bulk-like behavior than in NaY.

At temperatures above 250 K, the trends in the data for $A'_\mu(T)$ in Figure 7 for both NaY and USY suggest that they could be merging to a common value of ∼90 MHz, which is well above that expected from the free rotor result of $^1/_3[A'_\mu(0) + 2A'_\mu(120)]$ either in the bulk (58.0 MHz from the UMP2/EPR-III calculations[18]) or in NaY (62.7 MHz from Table 4). This signifies the onset of desorption of the butyl radical from its binding sites in both NaY and USY, which is consistent with the difficulty of seeing the Δ_1 resonance near 300 K (Figure 5) and also reinforces the earlier suggestion that the BEs of *t*-butyl to

dx.doi.org/10.1021/jp406879t | J. Phys. Chem. C 2013, 117, 16523−16539

cation sites in NaY are much less than for the cyclohexadienyl radical.[13]

The hfcc for the methyl (green diamonds) and methylene (cyan diamonds) protons, $A_{p,CH_3}(T)$ and $A_{p,CH_2Mu}(T)$, for Mu-*t*-butyl in NaY, plotted in Figure 8, are compared there with similar data from Figure 4 in the bulk (red and purple triangles). The dark-green trend line showing the $A_{p,CH_3}(T)$ dependence is not a separate fit to the NaY data but is the same fitted line as for the data in the bulk, with the same torsional barrier of 100 J/mol. This accounts as well for the data in NaY along with the two EPR points shown, which was confirmed by a separate fit giving V_2 = 98 J/mol.

The cyan line in Figure 8 is a fit to the $A_{p,CH_2Mu}(T)$ dependence for the NaY data only. The fit is from the B3LYP/H-capping calculations of Table 3, with $A_p(0)$ = 26.7 MHz, giving a fitted barrier of 2.6 ± 0.3 kJ/mol, which is similarly within errors as that determined over the full temperature range in the bulk (Figure 4) and gives a good account of all of the data points. The results for OH-capping are similar, with the same fitted barrier. The magenta line in Figure 7 is the fit line from the data for $A_{p,CH_2Mu}(T)$ only in the bulk. A comparison with the cyan fit line for the same dependence in NaY shows that the latter is clearly reduced compared to the bulk by a comparable amount as seen for $A'_\mu(T)$ in Figure 7, particularly at the lower temperatures. Although such a result is to be expected and is consistent with the transfer of some electron spin density from the central $\dot{C}$ of the radical to the Na cation, it is also a nice success of the theory that the same trend is so well reproduced here.

5.3. Sodium hfcc. The T dependence of the Na hfcc, $A_{Na}(T)$, is plotted (red triangles) in Figure 9. The calculations of Na hfcc (Tables 3 and 4) have assumed a static zeolite fragment, Si_6O_6Na, including the Na. This assumption is based on the powder neutron diffraction results of ref 40, showing only small changes in the interaction distances to the Na^+ in bare NaY as well as in the *t*-butyl·NaY distance between 4 and ∼298 K. Thus, we might have expected to see a T-independent Na hfcc. However, that is clearly not what the data is showing. The colored lines in Figure 9 are phenomenological fits that assume the same T dependence as in the dihedral angle dependence of eq 9 for the *t*-butyl radical but with the second term treated as a fitting parameter. Given the assumption of a static cation here, the only mechanism for altering the amount of electron spin density transferred to the Na^+ with temperature has to come from the T dependence of the dihedral motion either of the p_z orbital on the $-\dot{C}(CH_3)_2$ group, where the α-carbon is interacting with the cation in NaY (Table S2), or of the C−Mu bond in $-CH_2Mu$ with respect to p_z. In the simple classical model of twofold rigid-rotation that eq 6 represents, these motions are equivalent. In either case, the Na hfcc $A_{Na}(T)$ should exhibit the same T dependence as the muon in $A'_\mu(T)$.

The blue and red lines are the B3LYP/EPR-III calculations from Table 3 for this dihedral motion for OH-capping (124.4 MHz at 0 K) and H-capping (120.7 MHz), whereas the green line is from the UMP2/EPR-II H-capping calculations of Table 4 (79.8 MHz). The B3LYP fits cannot be distinguished, with both giving excellent fits to the data and the same torsional barrier of V_2 = 2.1 ± 0.2 kJ/mol. The data point at 30 K, with a hfcc of 118 MHz, albeit with a large error of ±8 MHz, provides a clear distinction between the B3LYP and UMP2 H-capping calculations of Table 4. The UMP2-calculated result (green line) gives a worse χ^2 with an anomalously high torsional barrier of V_2 = 4.4 ± 0.4 kJ/mol.

Of more interest perhaps, is the amount of electron spin-population transferred to the Na atom. We can estimate this from the results at 0 K in Figure 9. The trend in the data is in excellent agreement with the B3LYP-calculated fits and their values at 0 K, which average to $A_{Na}(0)$ ∼122 MHz. This would correspond to a spin population of about 14%, which is scaled from the maximum spin density of 886 MHz expected for the isolated Na atom.[65] Mulliken spin populations from the current calculations are given in Tables S4 and S5. For the B3LYP calculations with either H- or OH-capping, these are about 10%, which is in quite good agreement with the estimate above, particularly in view of a larger level of calculational error to be expected from the Pople 6-31+G** basis set used for the Na^+ and six-membered ring fragment for NaY. This is more restrictive than either the B3LYP/EPR-III or UMP2/EPR-II basis sets used for the *t*-butyl radical in the zeolite environment. To the best of our knowledge, the T dependence plotted for $A_{Na}(T)$ in Figure 9 and the spin population determined at 0 K is the only example of its kind for a nuclear hfcc (other than H) in zeolites. An earlier report in CuZSM5 determined the Cu hfcc at only a single high temperature of 433 K.[22]

6. CONCLUDING REMARKS

Reported in this Article is a detailed study of the temperature dependences of the muon and β-proton hyperfine coupling constants (hfcc) for the muoniated *t*-butyl radical in the bulk, down to low temperatures (5 K) for the first time, and also for the first time in the faujasitic zeolites NaY and USY. The muon hfcc of the more weakly formed Mu-isobutyl radical in the bulk have also been determined for the first time.

For both muoniated radicals but particularly for Mu-*t*-butyl, comparisons are made with single-molecule ab initio calculations at 0 K for the muon and proton hfcc from both B3LYP/EPR-III (Table 3) and UMP2/EPR-II (Table 4) calculations. The proton hfcc are calculated using the optimized geometry for the unsubstitued radical and are in better agreement with the B3LYP calculations, which is in accord with expectation.[18] Those for the muon are based on a simple ansatz for both methodologies, wherein the C−Mu bond is stretched by 1.076 to account qualitatively for the effect of vibrational averaging on the muon hfcc. Better agreement is found with the UMP2 calculations in the absence of evidence that intermolecular interactions impact on the muon hfcc, which also is in accord with this expectation.

The temperature dependence of the muon hfcc, $A'_\mu(T)$, and proton hfcc, $A_p(T)$, is modeled by a simple classical twofold potential, $V_2(\theta)$, for the dihedral angle dependence, with calculated hfcc at the equilibrium angles (0 and ±120°) weighted by a Boltzmann distribution of energy states to estimate the torsional barier to internal rotation. This simple model gives a good account of the experimental data in both the bulk and in NaY (Figures 3, 4, 7, and 8), with the only exception being the data for $A'_\mu(T)$ for *t*-butyl in the bulk, which exhibit a marked discontinuity at the (133 K) melting point of isobutene (Figure 3). This cannot be accounted for by a thermal average model, although good fits to $A'_\mu(T)$ are obtained separately in the solid and liquid phases.

An important feature of the present data in the faujasites, which stands in marked contrast to the data in the bulk, is that there is no discontinuity in $A'_\mu(T)$ at the bulk melting point in either NaY or USY (Figure 7), demonstrating that there is no equivalent to a macroscopic melting phenomena at a loading of three isobutenes/SC, but instead that local guest−host

dx.doi.org/10.1021/jp406879t | J. Phys. Chem. C 2013, 117, 16523−16539

interactions dominate at single binding sites in the supercage of the host lattice.

The proton hfcc for both the methyl and methylene ($-CH_2Mu$) protons of Mu-*t*-butyl show not only the lack of any discontinuity at the bulk melting point (Figure 4), in clear contrast to $A'_\mu(T)$, but also only small differences in the values for $A_{p,CH_3}(T)$ or $A_{p,CH_2Mu}(T)$ in NaY and the bulk (Figure 8). These comparisons, along with the observation of a continuous T dependence for $A'_\mu(T)$ in both zeolite frameworks, signal that the origin of the phase-dependent differences seen for the muon hfcc in the bulk lie in the specific intermolecular interactions with the C−Mu bond that influence the degree of vibrational averaging for the muon hfcc, leading to specifically enhanced hfcc in the solid phase.

The data for $A'_\mu(T)$ in NaY at lower temperatures falls below that in the bulk, a trend that is well reproduced by the UMP2 calculations in Figure 7, indicating the transfer of electron spin density to the Na cation. This trend is also seen in the proton hfcc for $A_{p,CH_2Mu}(T)$ in NaY in Figure 8, which is also well reproduced by theory. The Na hfcc from this spin density transfer, $A_{Na}(T)$, are plotted in Figure 9 and provide an estimate of the Na spin population, which agrees well with the calculated Mulliken values (Tables S3 and S4).

Even in cases where molecular interactions are expected, particularly in the many-body environment of the bulk, the single-molecule calculations of hfcc employed here, in concert with a simple rigid-rotor model for the torsional potential, do surpisingly well in accounting for the experimental data both in the bulk and in NaY (USY), with the exception of $A'_\mu(T)$ at the bulk-phase transition in Figure 3. To the best of our knowledge, this study and the one reported earlier for *s*-butyl radicals in ref 12 are the only examples utilizing ab initio calculations of hfcc to fit experimental data for muoniated alkyl radicals, not only in zeolites but also in the bulk.

■ ASSOCIATED CONTENT

Supporting Information

Geometric parameters for the *t*-butyl radical for its interaction with Na^+ and with NaY (H-capping) from UMP2/EPR-II calculations; binding energies for *t*-butyl interacting with Na^+, NaY (H-capping), and NaY(OH-capping) for different levels of calculations; Mulliken spin densities for different environments of the *t*-butyl and Mu-*t*-butyl radical interacting with Na^+ and NaY (H-capping) from B3LYP/EPR-III calculations; Mulliken spin densities for the UMP2/EPR-II calculations; and UMP2/EPR-III-calculated hyperfine coupling constants for *t*-butyl and Mu-*t*-butyl interacting with a bare Na cation. This material is available free of charge via the Internet at http://pubs.acs.org.

■ AUTHOR INFORMATION

Corresponding Author

*E-mail: flem@triumf.ca.

Notes

The authors declare no competing financial interest.

■ ACKNOWLEDGMENTS

We would like to thank the technical support staff of the Center for Molecular and Materials Sciences at TRIUMF and Dr. Khashayar Ghandi (now at Mt. Allison University) for his early participation in the data taking. The Natural Sciences and Engineering Research Council of Canada (NSERC) is also gratefully acknowledged for its financial support.

■ REFERENCES

(1) Roduner, E.; Percival, P. W.; Fleming, D. G.; Hochmann, J.; Fischer, H. Muonium-Substituted Transient Radicals Observed by Muon Spin Rotation. *Chem. Phys. Lett.* **1978**, *57*, 37−40.

(2) Atherton, N. M. *Principles of Electron Spin Resonance*; Ellis Horwood: New York, 1993.

(3) Percival, P. W.; Brodovitch, J. C.; Leung, S. K.; Yu, D.; Kiefl, R. F.; Luke, G. M.; Venkateswaran, K.; Cox, S. F. J. Intramolecular Motion in the Tert-butyl Radical as Studied by Muon Spin Rotation and Level-Crossing Spectroscopy. *Chem. Phys.* **1988**, *127*, 137−147.

(4) Roduner, E.; Strub, W.; Burkhard, P.; Hochmann, J.; Percival, P. W.; Fischer, H.; Ramos, M.; Webster, B. C. Muonium Substituted Organic Free-Radicals in Liquids - Muon Electron Hyperfine Coupling-Constants of Alkyl and Allyl Radicals. *Chem. Phys.* **1982**, *67*, 275−285.

(5) Paul, H.; Fischer, H. Electron-Spin Resonance of Free-Radicals in Photochemical Reactions of Ketones in Solution. *Helv. Chim. Acta* **1973**, *56*, 1575−1594.

(6) Krusic, P. J.; Jesson, J. P.; Meakin, P. Electron Spin Resonance Studies of Conformations and Hindered Internal Rotation in Transient Free Radicals. *J. Phys. Chem.* **1971**, *75*, 3438−3453.

(7) (a) Fessenden, R. W.; Schuler, R. H. Electron Spin Resonance Studies of Transient Alkyl Radicals. *J. Chem. Phys.* **1963**, *39*, 2147−2195. (b) Fessenden, R. ESR Studies of Internal Rotation in Radicals. *J. Chim. Phys. Phys.−Chim. Biol.* **1964**, *61*, 1570−1575.

(8) Fischer, H. Electron Spin Resonance of Transient Alkyl Radicals during Alkyllithium-Alkyl Halide Reactions. *J. Phys. Chem.* **1969**, *73*, 3834−3838.

(9) Roduner, E. Muon Spin Resonance - A Variant of Magnetic Resonance. *Appl. Magn. Reson.* **1997**, *13*, 1−14.

(10) Roduner, E., The Positive Muon as a Probe in Free Radical Chemistry. In *Lecture Notes in Chemistry*; Springer Verlag: New York, 1988; Vol. *49*.

(11) Roduner, E. Polarized Positive Muons Probing Free-Radicals: A Variant of Magnetic-Resonance. *Chem. Soc. Rev.* **1993**, *22*, 337−346.

(12) Fleming, D. G.; Bridges, M. D.; Arseneau, D. J.; Chen, Y. K.; Wang, Y. A. Isotope Effects and the Temperature Dependences of the Hyperfine Coupling Contants of Muoniated sec-Butyl Radicals in Condensed Phases. *J. Phys. Chem A* **2011**, *115*, 2778−2793.

(13) Fleming, D. G.; Arseneau, D. J.; Shelley, M. Y.; Beck, B.; Dilger, H.; Roduner, E. μSR Studies of Hyperfine Couplings and Molecular Interactions of the Mu-Cyclohexadienyl Radical in Y-Zeolites and in Solid Bulk Benzene. *J. Phys. Chem. C* **2011**, *115*, 11177−11191.

(14) Fleming, D. G.; Pan, J. J.; Senba, M.; Arseneau, D. J.; Kiefl, R. F.; Shelley, M. Y.; Cox, S. F. J.; Percival, P. W.; Brodovitch, J. C. Spin Relaxation of Muonium-Substituted Ethyl Radicals ($MuCH_2CH_2^\bullet$) in the Gas Phase. *J. Chem. Phys.* **1996**, *105*, 7517−7535.

(15) Martyniak, A.; Dilger, H.; Scheuermann, R.; Tucker, I. M.; McKenzie, I.; Vujosevic, D.; Roduner, E. Using Spin Polarised Positive Muons for Studying Guest Molecule Partitioning in Soft Matter Structures. *Phys. Chem. Chem. Phys.* **2006**, *8*, 4723−4740.

(16) Bridges, M. D.; Arseneau, D. J.; Fleming, D. G.; Ghandi, K. Hyperfine Interactions and Molecular Motion of the Mu-Ethyl Radical in Faujasites: NaY, HY, and USY. *J. Phys. Chem. C* **2007**, *111*, 9779−9793.

(17) Kaprinidis, N. A.; Landis, M. S.; Turro, N. J. Supramolecular Control of Photochemical Enantiomeric Induction and Radical Pair Recombintion in Zeolites. *Tetrahedron Lett.* **1997**, *38*, 2609−2612.

(18) Chen, Y. K; Fleming, D. G.; Wang, Y. A. Theoretical Calculations of Hyperfine Coupling Constants for Muoniated Butyl Radicals. *J. Phys. Chem. A* **2011**, *115*, 2765−2777.

(19) Fleming, D. G.; Shelley, M. Y.; Arseneau, D. J.; Senba, M.; Pan, J. J.; Roduner, E. Hyperfine and Host-Guest Interactions of the Mu-cyclohexadienyl Radical in NaY Zeolite. *J. Phys. Chem. B* **2002**, *106*, 6395−6407.

(20) Roduner, E.; Stolmar, M.; Dilger, H.; Reid, I. D. Reorientational Dynamics of Cyclohexadienyl Radicals in High-Silica ZSM-5. *J. Phys. Chem. A* **1998**, *102*, 7591−7597.

(21) Roduner, E.; Dilger, H. M. Acid Catalyis in HZSM-5: The Role of Entropy. *J. Am. Chem. Soc.* **2001**, *123*, 7717−7718.

(22) Stolmar, M.; Roduner, E. Complexation of Copper by Cyclohexadienyl Radicals in Cu/ZSM-5 Zeolite. *J. Am. Chem. Soc.* **1998**, *120*, 583−584.
(23) Jacobs, P. A.; Martens, J. A. *Introduction to Zeolite Science and Practice*; van Bekum, H., Flaningen, E. M., Jansen, J. C., Eds.; Elsevier: Amsterdam, 1991.
(24) *Modelling of Structure and Reactivity in Zeolites*; Catlow, C. R. A., Ed.; Academic Press: London, 1992.
(25) (a) Vos, A.; Rosanska, X.; Schoonheydt, R. A.; Hutschka, H.; Hafner, J. A Theoretical Study of the Alkylation Reaction of Tolune with Methanol Catalyzed by Acidic Mordenite. *J. Am. Chem. Soc.* **2001**, *123*, 2799−2809. (b) *Molecular Transport and Reaction in Zeolites: Design and Application of Shape Selective Catalysts*; Chen, N. Y., Degnan, T. F., Jr., Smith, C. M., Eds.; VCH Publishers: New York, 1994; pp 195−289.
(26) Haw, J. F. Zeolite Acid Strength and Reaction Mechanisms in Catalysis. *Phys. Chem. Chem. Phys.* **2002**, *4*, 5431−5441.
(27) Barthomeuf, D. Basic Zeolites: Characterization and Reaction Mechansims in Catlysis. *Catal. Rev.* **1996**, *38*, 521−612.
(28) Venutuo, P. B. Structure-Reactivity-Selectivity Relationships in Reaction of Organics over Zeolite Catlysts. *Stud. Surf. Sci. Catal.* **1997**, *105*, 811−852.
(29) Rosanska, X.; van Santen, R. A.; Demuth, T.; Hutschka, F.; Hafner, J. A Periodic DFT Study of Isobutene Chemisorption in Proton-Exchanged Zeolites: Dependence of Reactivity on the Zeolite Framework Structure. *J. Phys. Chem. B* **2003**, *107*, 1309−1315.
(30) Carley, A. F.; Edwards, H. A.; Mile, B.; Wyn Roberts, M.; Rowlands, C. G.; Hancock, F. E.; Jackson, D. S. Application of EPR to a Study of the Hydrogenation of Ethene and Benzene Over a Supported Pd Catalyst: Detection of Free radicals on a Catalyst Surface. *J. Chem. Soc., Faraday Trans.* **1994**, *90*, 3341−3346.
(31) Werst, D. W.; Han, P.; Choure, S. C.; Vinokur, E. I.; Xu, L.; Trifunac, A. D.; Eriksson, L. A. Hydrogen Atom Addition to Hydrocarbon Guests in Radiolyzed Zeolites. *J. Phys. Chem. B* **1999**, *103*, 9219−9230.
(32) (a) Ramos, M. J.; Mckenna, D.; Webster, B. C.; Roduner, E. Muon Spin Rotation Spectra for Muonium Isotopically Substituted Ethyl Radicals. *J. Chem. Soc., Faraday Trans. 1* **1984**, *80*, 255−265. (b) Ramos, M. J.; Mckenna, D.; Webster, B. C.; Roduner, E. The Barriers to Internal Rotation for Muonic-Substituted Ethyl Radicals. *J. Chem. Soc., Faraday Trans. 1* **1984**, *80*, 267−274.
(33) (a) Claxton, T. A.; Graham, A. M. Ab Initio Study of Propyl Radicals. *J. Chem. Soc., Faraday Trans. 2* **1988**, *84*, 121−134. (b) Claxton, T. A.; Graham, A. M. A Chemical Interpretation of Vibrationlly Induced Barriers to Hindered Internal Rotation. *J. Chem. Soc., Faraday Trans. 2* **1987**, *83*, 2307−2317.
(34) Webster, B.; Buttar, D. Vibrational Behaviour of the Carbon-Muonium Bond in the Muonated Ethyl Radical. *J. Chem. Soc., Faraday Trans.* **1996**, *92*, 2331−2334.
(35) Ghandi, K.; Zahariev, F. E.; Wang, Y. A. Theoretical Studies of Alkyl Radicals in the NaY and HY Zeolites. *J. Phys. Chem. A* **2005**, *109*, 7242−7250.
(36) Suter, H. U.; Ha, T. K. A Theoretical-Study on the Internal-Rotation and Hyperfine Structures of the Ethyl Radical (CH_3-CH_2). *Chem. Phys.* **1991**, *154*, 227−236.
(37) Chipman, D. M. Theoretical-Study of Hyperfine Coupling-Constants in Ethyl Radical. *J. Chem. Phys.* **1991**, *94*, 6632−6637.
(38) Carmichael, I. Ab Initio Quadratic Configuration-Interaction Calculation of the Isotropic Hyperfine Coupling-Constants in the Ethyl Radical. *J. Phys. Chem.* **1991**, *95*, 6198−6201.
(39) (a) Pacansky, J.; Yoshimine, M. Theoretical-Studies on the Barriers for Internal-Rotation of the Methyl-Groups in the Tert-Butyl Radical. *J. Phys. Chem.* **1986**, *90*, 1980−1983. (b) Yoshimine, M.; Pacansky, J. Theoretical-Studies on the Structure of Isobutane and the Tertiary-Butyl Radical. *J. Chem. Phys.* **1981**, *74*, 5168−5173.
(40) Fitch, A. N.; Jobic, H.; Renourprez, A. J. Localization of Benzene in Sodium-Y Zeolite by Powder Neutron Diffraction. *J. Phys. Chem.* **1986**, *90*, 1311−1318.
(41) Henson, N. J.; Eckert, J.; Hay, P. J.; Redondo, A. Adsorption of Ethane and Ethene in NaY Zeolite- Computational Study and Comparison with Benzene. *Chem. Phys.* **2000**, *261*, 111−124.
(42) (a) Macrae, R. M.; Webster, B. Orientation and Binding of Cyclohexadienyl Radical in NaY Zeolite−Computational Study and Comparison with Benzene. *Phys. B* **2003**, *326*, 68−71. (b) Webster, B.; Macrae, R. M. A Theoretical Investigation of the Effect of Na Cation on the Proton-Electron Hyperfine Coupling Constants of the Cyxlohexadienyl Radical and Some Consequences for the Muonium-Substituted Cyclohexadienyl Radical, C_6H_6Mu, Formed in Zeolite. *Phys. B* **2000**, *289*, 598−602.
(43) Senba, M.; Fleming, D. G.; Arseneau, D. J.; Garner, D. M.; Reid, I. D. Muonium Depolarization by Electron-Spin Exchange with O2 Gas in the Temperature-Range 90−500 K. *Phys. Rev. A* **1989**, *39*, 3871−3883.
(44) Kreitzman, S. R.; Roduner, E. Theory of Avoided Level-Crossing Relaxation Dynamics for Axial Muonated Radicals. *Chem. Phys.* **1995**, *192*, 189−230.
(45) Senba, M.; Arseneau, D. J.; Pan, J. J.; Fleming, D. G. Slowing-Down Times and Stopping Powers for ∼ 2-MeV μ^+ in Low-Pressure Gases. *Phys. Rev. A* **2006**, *74*, 042708−042724.
(46) Ghandi, K.; Bridges, M. D.; Arseneau, D. J.; Fleming, D. G. Muonium Formation as a Probe of Radiation Chemistry in Sub- and Supercritical Carbon Dioxide. *J. Phys. Chem. A* **2004**, *108*, 11613−11625.
(47) Duchovic, R. J.; Wagner, A. F.; Turner, R. E.; Garner, D. M.; Fleming, D. G. The Analysis of Muonium Hyperfine Interaction Measurements of Thermal Rate Constants for Addition-Reactions. *J. Chem. Phys.* **1991**, *94*, 2794−2806.
(48) Percival, P. W.; Brodovitch, J. C.; Arseneau, D. J.; Senba, M.; Fleming, D. G. Formation of the Muoniated Ethyl Radical in the Gas Phase. *Phys. B* **2003**, *326*, 72−75.
(49) (a) Heming, M.; Roduner, E. Formation and Dynamics of a SiO2-Adsorbed Radical Observed by Muon Spin Rotation. *Surf. Sci.* **1987**, *189*, 535−542. (b) Heming, M. Modern EPR-Related Methods in Surface Science and Heterogeneous Catalysis. *Z. Phys. Chem.* **1987**, *151*, 35−50.
(50) Krusic, P. J.; Meakin, P. Barrier to Pyramidal Inversion in Tert-Butyl Radical by Electron-Spin Resonance. *J. Am. Chem. Soc.* **1976**, *98*, 228−230.
(51) Improta, R.; Barone, V. Interplay of Electronic, Environmental, and Vibrational Effects in Determining the Hyperfine Coupling Constants of Organic Free Radicals. *Chem. Rev.* **2004**, *104*, 1231−1253.
(52) Hermosilla, L.; Calle, P.; de la Vega, J. M. G.; Sieiro, C. Density Functional Theory Predictions of Isotropic Hyperfine Coupling Constants. *J. Phys. Chem. A* **2005**, *109*, 1114−1124.
(53) Barone, V. Structure, Magnetic Properties and Reactivities of Open-Shell Species from Density Functional and Self-Consistent Hybrid Methods. In *Recent Advances in Density Functional Methods*; Chong, D. P., Ed.; World Scientific Publication Co.: River Edge, NJ, 1996; Chapter 8, pp 287−334.
(54) Barone, V. Anharmonic Vibrational Properties by a Fully Automated Second-Order Perturbative Approach. *J. Chem. Phys.* **2005**, *122*, 014108−014117.
(55) Thomas, S. L.; Carmichael, I. Hyperfine Interactions in Muonium-Containing Radicals. *Phys. B* **2006**, *374*, 290−294.
(56) Böhm, M. C.; Ramirez, R.; Schulte, J. Finite-Temperature Properties of the Muonium Substituted Ethyl Radical CH(2)MuCH(2): Nuclear Degrees of Freedom and Hyperfine Splitting Constants. *Mol. Phys.* **2005**, *103*, 2407−2436.
(57) Claxton, T. A.; Graham, A. M.; Cox, S. F. J.; Maric, D. M.; Meier, P. F.; Vogel, S. Vibrationally Averaged Spin-Densities on Muons and Protons in the Hydroxyl and Ethyl Radicals. *Hyperfine Interact.* **1990**, *65*, 913−926.
(58) Lounila, J.; Wasser, R.; Diehl, P. Effects of Anharmonic Vibrations on Molecular-Properties. *Mol. Phys.* **1987**, *62*, 19−31.
(59) Johnson, P. M.; Sears, T. J. Vibrational Effects on the Torsional Motion of Ethyl Radical. *J. Chem. Phys.* **1999**, *111*, 9222−9226.
(60) Mitov, S.; Panchenko, A.; Roduner, E. Spin Polarization, Delocalization, and the Effect of Nonplanarity in Hyperfine Coupling

Constants of Perfluorinated Alkyl Radicals. *J. Phys. Chem. A* **2007**, *111*, 5294−5299.
(61) Frisch, M. J; Trucks, G. W; Schlegel, H. B; Scuseria, G. E; Robb, M. A; Cheeseman, J. R; Scalmani, G.; Barone, V.; Mennucci, B.; Petersson, G. A; et al. *Gaussian09*, revision A.02; Gaussian, Inc.: Wallingford, CT, 2009.
(62) Becke, A. D. Density Functional Themochemistry. III. The Role of Exact Exchange. *J. Chem. Phys.* **1993**, *98*, 5648−5672.
(63) Lee, C.; Yang, W.; Parr, R. G. Development of the Colle-Salvetti Correlation-Energy Formula Into a Functional of the Electron Density. *Phys. Rev. B* **1988**, *37*, 785−789.
(64) Toriyama, K.; Iwasaki, M.; Nunome, K.; Muto, H. An ESR and ENDOR Study of Tunneling Rotation of a Hindered CH_3 Group in C_2H_5. *J. Chem. Phys.* **1981**, *75*, 1633−1638.
(65) Weltner,W. *Magnetic Atoms and Molecules*; Dover Publications, New York, 1983; p 22.